MARTIN

J. Fluid Mech. (1994), *vol.* 258, *pp.* 31–75

Velocity measurements in a high-Reynolds-number, momentum-conserving, axisymmetric, turbulent jet

By HUSSEIN J. HUSSEIN†, STEVEN P. CAPP‡ AND WILLIAM K. GEORGE

Turbulence Research Laboratory, Department of Mechanical and Aerospace Engineering, State University of New York at Buffalo, Buffalo, NY 14260, USA

(Received 29 March 1990 and in revised form 24 May 1993)

The turbulent flow resulting from a top-hat jet exhausting into a large room was investigated. The Reynolds number based on exit conditions was approximately 10^5. Velocity moments to third order were obtained using flying and stationary hot-wire and burst-mode laser-Doppler anemometry (LDA) techniques. The entire room was fully seeded for the LDA measurements. The measurements are shown to satisfy the differential and integral momentum equations for a round jet in an infinite environment.

The results differ substantially from those reported by some earlier investigators, both in the level and shape of the profiles. These differences are attributed to the smaller enclosures used in the earlier works and the recirculation within them. Also, the flying hot-wire and burst-mode LDA measurements made here differ from the stationary wire measurements, especially the higher moments and away from the flow centreline. These differences are attributed to the cross-flow and rectification errors on the latter at the high turbulence intensities present in this flow (30% minimum at centreline). The measurements are used, together with recent dissipation measurements, to compute the energy balance for the jet, and an attempt is made to estimate the pressure–velocity and pressure–strain rate correlations.

1. Introduction

The axisymmetric jet (shown schematically in figure 1) represents a benchmark for research into the physics of turbulent fluid flow. Although experimental methods are complicated by the high local turbulence intensities of this flow, the theoretical study is simplified since the jet is both axisymmetric in the mean and a free shear flow to which boundary-layer approximations can be applied. The axisymmetric jet's importance to the understanding of turbulence is evidenced by the volumes of publications involving experimental data, mathematical analysis, and computational modelling (e.g. the reviews by Monin & Yaglom 1971; Hinze 1975; Townsend 1976; Rodi 1975*a*; List 1979).

Early experimental investigations of the jet include the work of Corrsin (1943), Corrsin & Uberoi (1950, 1951), Reichardt (1941), Hinze & van der Hegge Zijnen (1949), and Corrsin & Kistler (1955). The failure of the turbulence intensities to attain self-preservation in these early works motivated the efforts of Wygnanski & Fielder (1969) using linearized hot-wires. Their work became the standard reference for the quantitative description for profiles of mean velocities, turbulence stresses and triple

† Present address: Vanderbilt University, Nashville, TN, USA.
‡ Present address: Harrison Radiator Division, General Motors Corp., Lockport, NY, USA.

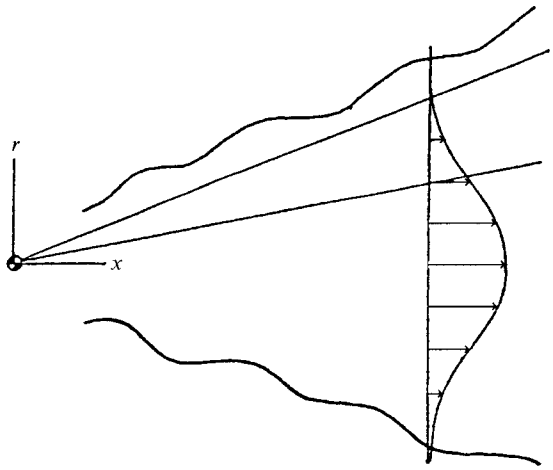

FIGURE 1. Axisymmetric jet coordinates.

correlation coefficients. Rodi (1975*a*) and List (1980) provide useful reviews of these studies.

Occasionally researchers have utilized the far field of the jet to evaluate new experimental methods or to examine the role of large-scale structures, thereby expanding the database. For example, Rodi (1975*b*), investigating a new technique for analysing hot-wire signals, measured first and second moments at positions up to 75 diameters from the jet exit. Lehrmann (1986) used different laser Doppler anemometer (LDA) seeding techniques to examine the entrainment process and in the course of the investigation obtained profiles of mean velocity and turbulence intensities. Neither of these experiments obtained profiles which agreed particularly well with the earlier measurements which used more conventional techniques.

The jet has also been heavily studied by turbulent modellers. Tollmien's (1926) study based on Prandtl's mixing-length theory was the first of many theoretical treatments of the circular jet. In fact, the difficulties of predicting this flow with model constants determined from other flows has proved to be one of the more challenging problems faced by turbulence modellers over the past two decades. These efforts have been reviewed in detail by Hinze (1975), Rodi (1975*a*), and more recently by Taulbee (1989).

Questions concerning the validity of the jet data as determined by the equations of motion were first raised at the Turbulence Research Laboratory of SUNY/Buffalo during the late 1970s. Baker (1980), while investigating the evolution of a hot axisymmetric turbulent jet into a turbulent plume using numerical methods, discovered that the far-field data of Wygnanski & Fiedler (1969) failed to satisfy the constraint of the integrated axial momentum equation. Seif (1981) in a subsequent numerical study, using both $k-\epsilon$ and Reynolds stress models, also found significant problems with that data. These difficulties prompted the experimental study by Capp (1983) using LDA techniques to investigate this constraint in order to clarify the source of the discrepancy. Those measurements established that the error was facility-related and that there can be significant differences between a jet in a confined or semi-confined enclosure and one in an infinite environment because of the recirculating flow entrained by the jet. All of these results have been discussed in detail by Capp & George (1982), George *et al.* (1982, 1988), and George (1990), as well as in the reference cited above.

There have also been several recent re-examinations of jet theory. Schneider (1985) analysed the entire flow field (including the entrainment region) with a multiple scaling

approach using inner and outer expansions. He was able to show that the integrated momentum flux at each cross-section of the axisymmetric jet remained constant to first order and equal to the rate at which momentum was added at the source. This was quite unlike the plane jet where the boundary conditions in the vicinity of the source significantly modified the integrated momentum from its source value. In a complementary study, George *et al.* (1982) showed from scaling arguments that the integrated momentum equation was constant to second order at the source value. This constraint imposed by the integrated momentum equations will be discussed in detail later, and will be seen to form an important criterion for validating the experiment.

The possibility of self-preserving solutions to the axisymmetric jet equations was recognized by Tollmien (1926) and others. All of the texts cited above review the principles of self-preservation as applied to this flow (see also Tennekes & Lumley 1972 for a self-contained discussion). In brief, solutions to the averaged equations are sought which are of the form $U = U_s(x)f(\eta)$, $-\overline{uv} = R_s(x)g(\eta)$, etc., where $\eta = r/x$ and the coordinate system is shown in figure 1. If it is assumed that the flow can be scaled by a single length and velocity scale then it can be shown that self-preservation is possible only if $\mathrm{d}\delta/\mathrm{d}x$ is a constant, presumed universal. These assumptions can be justified from dimensional and physical arguments only if the source is presumed to be a point source of momentum only (cf. George 1989, Monin & Yaglom 1971). It has been widely accepted that all jets should asymptotically approach the same self-preserving state, independent of the details of their origin (cf. Townsend 1976).

Recently, George (1989) discovered a short-coming in the original similarity theory which implicitly assumed that the self-preserving state was independent of the details of the initial conditions. The more general analysis showed that the self-preserving state attained could be in fact uniquely determined by the initial conditions. It also reviewed that any x-variation of the jet transverse lengthscale δ for which $R_s/U_s^2/\mathrm{d}\delta/\mathrm{d}x =$ constant can result in a self-preserving jet, at least at the order of the mean momentum equation. Only by considering the consequences of self-preservation on the higher-order moments can the linear growth rate be recovered, but even then with coefficients determined by the details of the initial conditions (especially exit profile and Reynolds number). The new results make it clear that the laboratory jets can never approximate the point-source of momentum jets of the earlier analysis, and that each class of laboratory jet is in principle asymptotically unique (e.g. top-hat jets, fully-developed pipe flow jets, etc.), and retain forever a dependence on the source Reynolds number. The arguments leading to these conclusions and their implications for the higher moments are summarized in Appendix C.

This paper reports the results of an experimental program to measure the velocity moments (to third order) of an axisymmetric jet. Both stationary and flying hot-wire (referred to as SHW and FHW respectively) and burst-mode LDA techniques were used for the same source and boundary conditions. The data obtained have been analysed together with the governing equations and boundary conditions believed to apply to the axisymmetric jet. It will be argued that since the flying hot-wire and burst-mode LDA results alone satisfy these equations, the stationary hot-wire results reported here (and many of the experiments performed earlier) are not representative of an axisymmetric jet. (too high turbulence intensity for stationary wires)

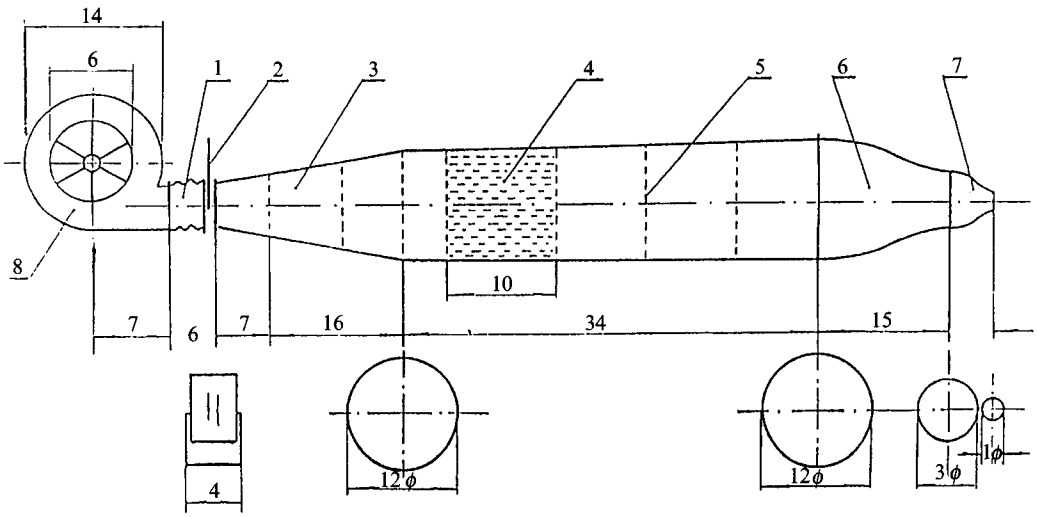

FIGURE 2. Schematic of jet apparatus. 1. Vibration isolation; 2. slot and plate; 3. diffuser; 4, honeycomb; 5. screen; 6. nozzle; 7. jet; 8. blower. (Dimensions in inches.)

Quantity	Symbol	Value
Exit diameter (inches)	D	1.0
Velocity (m/s)	U_0	56.2
volume flux (m^3/s)	m_0	0.0287
momentum × volume flux = Momentum flux/unit mass (m^4/s^2)	M_0	1.61 $\cdot \rho = [N]$
Reynolds number	Re_D	9.55×10^4

TABLE 1. Exit parameters

2. Experimental facility and the measurement hardware

2.1. *The jet*

The jet used in the experiments reported here was an existing facility modified to closely match the boundary conditions of Wygnanski & Fiedler. A schematic of the jet apparatus is shown in figure 2. Briefly, a paddle blower exhausted through a diffuser into a 12 in. diameter settling chamber which contained both honeycomb and screens. Two contractions were used to reach the jet exit diameter of 1 in. The first of these reduced the diameter to 3 in. and was of matched cubic design and the second was of fifth-order polynomial design.

A hot-wire probe was used to measure the mean velocity and turbulence intensity across the jet exit. Measurements were made along vertical and horizontal lines passing through the centre of the jet exit at 33 locations spaced $\frac{1}{16}$ in. apart. The average of the mean velocities for these points was 56.2 m/s with a standard deviation of 0.72 m/s. This value was accepted as the jet exit velocity U_0. The turbulence intensity at the exit was nominally 0.58%, the largest portion of which was at low frequency and related to the unsteadiness of the fan. Exit parameters for the jet are listed in table 1. The boundary layer at the jet lip was laminar with $\delta_{95} = 0.7$ mm. Because there was a slight increase in velocity with radius (2%) owing to the contraction, to an excellent approximation the jet could be considered to have a top-hat profile, and the exit

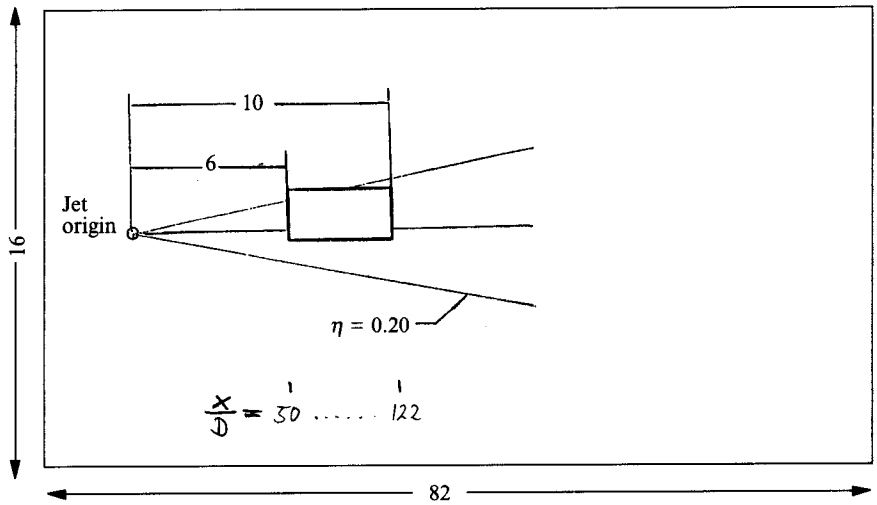

FIGURE 3. Schematic showing layout of jet facility. (Dimensions in feet.)

volume flux, ρm_0, and momentum flux, ρM_0, could be determined using the jet exit velocity, U_0, and exit diameter, D, i.e.

$$\rho m_0 = \tfrac{1}{4}\pi U_0 D^2, \tag{2.1}$$

and

$$\rho M_0 = \tfrac{1}{4}\pi U_0^2 D^2. \tag{2.2}$$

Since the jet nozzle was machined with an accuracy of 0.001 in., the major error term in the calculation of the exit momentum is due to the variation in the exit velocity. Using 0.72 m/s as the error estimator for the exit velocity, the uncertainty in the calculation of the rate of momentum addition at the source is approximately 2.6%. Note that an accurate description of the exit conditions is needed only for the normalization of the centreline velocity, U_c, since all transverse profiles are non-dimensionalized with respect to it.

2.2. *The enclosure*

In order to provide uniform spatial seeding for the LDA measurements, the jet facility was surrounded by a large enclosure constructed of polythene sheet. The enclosure was designed to minimize the backflow momentum so that the jet retained 90% of its momentum to $x/D = 200$ using the criterion proposed by Capp (1983). (This criterion is reviewed in Appendix B.) The enclosure (shown schematically in figure 3) was square in cross-section, having a width of 16 ft and a length of 82 ft. The jet was centred in the cross-section of the enclosure, the exit being 34 ft from the endwall. The traversing system was capable of moving 6 ft along the x-axis and 4 ft along both the y- and z-axes. It was positioned to take measurements from 50 to 122 exit diameters downstream.

2.3. *The hot-wire anemometry*

The hot-wire measurements were taken using standard Dantec 5 μm wire probes (55P01, 55P51 and 55P53) and 55M10 CTA units. The anemometer voltages were digitized using a Phoenix Data 15 bit A/D converter capable of 150 kHz throughput rate with simultaneous sample and hold on all channels. Probe calibration and data acquisition were done using a DEC PDP 11/84 minicomputer with a DEC RA81 500 Mbyte disk drive and a DEC TU81 high-speed tape drive. The hot wires were calibrated for velocity using the polynomial calibration law described by George *et al.*

Mean velocity ($V, W = 0$ by assumption)

Single wire

$$U_m = U\left\{1+\frac{1}{2}\frac{\overline{w^2}}{U^2}-\frac{1}{2}\frac{\overline{uw^2}}{U^3}+\frac{1}{2}\frac{\overline{u^2w^2}}{U^4}-\frac{1}{8}\frac{\overline{w^4}}{U^4}\cdots\right\}$$

Cross-wire

$$U_m = U\left\{1+\left(\frac{1}{1+k^2}\right)\frac{\overline{w^2}}{U^2}-\left(\frac{1}{1+k^2}\right)\frac{\overline{uw^2}}{U^3}+\ldots\right\}$$

$$V_m = U\left\{\frac{\overline{u^2v}}{U^3}+\left(\frac{2}{1+k^2}\right)\frac{\overline{vw^2}}{U^3}+\frac{\overline{u^3v}}{U^4}+\frac{5}{2}\left(\frac{2}{1+k^2}\right)\frac{\overline{uvw^2}}{U^4}+\ldots\right\}$$

Second central moments

Single wire

$$\overline{u_m^2} = \overline{u^2}+\frac{\overline{uw^2}}{U}-\frac{\overline{u^2w^2}}{U^2}+\frac{1}{4}\frac{\overline{w^4}-\overline{w^2}^2}{U^2}+\ldots$$

Cross-wire

$$\overline{u_m^2} = \left\{\overline{u^2}+\left(\frac{2}{1+k^2}\right)\frac{\overline{uw^2}}{U}-\left(\frac{2}{1+k^2}\right)\frac{\overline{u^2w^2}}{U^2}+\left(\frac{1}{1+k^2}\right)^2\frac{\overline{w^4}}{U^2}-\left(\frac{2}{1+k^2}\right)^2\frac{\overline{w^2}^2}{U^2}+\ldots\right\}$$

$$\overline{v_m^2} = \overline{v^2}+2\frac{\overline{u^2v^2}}{U^2}+2\left(\frac{2}{1+k^2}\right)\frac{\overline{v^2w^2}}{U^2}+2\frac{\overline{u^3v^2}}{U^3}+\ldots$$

$$\overline{u_m v_m} = \overline{uv}+\left(\frac{1}{1+k^2}\right)\left[\frac{\overline{vw^2}}{U}+\frac{\overline{uvw^2}}{U^2}\right]+\frac{\overline{u^3v}}{U^2}+\ldots$$

Third central moments

Single wire

$$\overline{u_m^3} = \overline{u^3}+\frac{3}{2}\frac{\overline{u^2w^2}-\overline{u^2}\,\overline{w^2}}{U}+\ldots$$

Cross-wire

$$\overline{u_m^3} = \overline{u^3}+\left(\frac{2}{1+k^2}\right)\left[-\frac{5}{2}\frac{\overline{u^2w^2}}{U}-\frac{1}{2}\frac{\overline{u^2}\,\overline{w^2}}{U}-\frac{3}{2}\frac{\overline{u^3w^2}}{U^2}+\frac{1}{2}\frac{\overline{u^2}\,\overline{uw^2}}{U^2}\right]$$
$$+\left(\frac{2}{1+k^2}\right)^2\left[\frac{3}{4}\frac{\overline{uw^4}}{U^2}-\frac{1}{2}\frac{\overline{w^2}\,\overline{uw^2}}{U^2}\right]+\ldots$$

$$\overline{v_m^3} = \overline{v^3}+3\left[\frac{\overline{u^2v^3}-\overline{v^2}\,\overline{u^2v}}{U^2}\right]+\left(\frac{2}{1+k^2}\right)\left[\frac{\overline{v^3w^2}-\overline{v^2}\,\overline{vw^2}}{U^2}\right]+\ldots$$

$$\overline{u_m v_m^2} = \overline{uv^2}+\left(\frac{1}{1+k^2}\right)\left[\frac{\overline{v^2w^2}-\overline{v^2}\,\overline{w^2}}{U}\right]+\left[\frac{2\overline{u^3v^2}-\overline{uv}\,\overline{u^2v}}{U^2}\right]$$
$$+\left(\frac{2}{1+k^2}\right)\left[\frac{3}{2}\frac{\overline{uv^2w^2}}{U^2}-\frac{\overline{uv}\,\overline{vw^2}}{U^2}+\frac{1}{2}\frac{\overline{v^2}\,\overline{uw^2}}{U^2}\right]+\ldots$$

$$\overline{u_m^2 v_m} = \overline{u^2v}+\left(\frac{2}{1+k^2}\right)\left[\frac{\overline{uvw^2}-\overline{uv}\,\overline{w^2}}{U}+\frac{2\overline{u^2vw^2}-\overline{uv}\,\overline{uw^2}-\overline{u^2}\,\overline{vw^2}}{U^2}\right]$$
$$+\left(\frac{1}{1+k^2}\right)^2\left[\frac{\overline{vw^4}-2\,\overline{vw^2}\,\overline{w^2}}{U^2}\right]$$

TABLE 2. Leading terms in hot-wire cross-flow errors

(1989), and for angle using the velocity dependent k-factor technique of Beuther, Shabbir & George (1987). The average accuracy of this calibration method was $\pm 0.1\%$. The flow-field data was transported via magnetic tape to a VAX for further processing.

In order to guarantee the statistical independence of each sample, the autocorrelation was measured directly and used to determine the integral scale at various locations across the flow. This was in turn used to set the sampling rate for the A/D at less than one sample every two integral scales so that each sample was effectively statistically independent (see George 1979). A total of 2000 independent samples at a rate of 13 Hz (total record length of 154 s) was taken at each position. This corresponds to a sampling error for the mean of approximately 3% at the outermost radial location and 0.7% at the centreline. The sampling error in the second and fourth moments for all locations is estimated at 3% and 20%, respectively.

An important limitation on the stationary hot-wire (hereinafter denoted as SHW) measurements of this investigation arises because of the high local turbulence intensity which is about 30% at the jet centreline and increases to greater than 100% past the velocity half-width. The effects of high turbulence intensity on hot wires have been discussed by a number of authors including Tutu & Chevray (1975), and Beuther *et al.* (1987). The principal limitations are cross-flow, rectification and drop-out, all of which increase with the turbulence intensity. Beuther *et al.* (1987) suggest that these effects can be assumed to be unimportant only as long as the leading terms are negligible in an expansion about a state of zero turbulence level. The expansions for the mean quantities of interest in this investigation are summarized in table 2. Note that the leading error terms for cross-wires are larger than for single wires, and that error terms for moments above the first enter at only one order above the moment being measured. The significance of these observations will be seen later when comparing the stationary hot-wire (SHW) results with those of the flying hot-wire (FHW) and burst-mode laser-Doppler anemometer (LDA).

2.4. *The flying hot-wire apparatus (FHW)*

The flying-wire experiments were performed by whirling the probes about an axis perpendicular to the axis of the jet. To decrease the interference of the supporting arm, the probes were mounted approximately 0.1 m away from the tip of a 1 m long, low-drag symmetric NACA 0010 airfoil. A one horse-power motor was used in combination with a set of reduction gears and counter weights to obtain smooth rotation of the wing. The entire mechanism was mounted on a one-dimensional manual traversing system which was used to move the probes across the jet. A sketch of the apparatus is shown in figure 4. Measurements which used the whirling wire system were taken on a radial traverse at a distance of 70 diameters downstream from a one-inch diameter axisymmetric air jet. The purpose of the flying wire was to reduce the cross-flow, rectification and drop-out errors associated with the high local turbulence intensity. Accordingly, the rotation rate was chosen to be 66 r.p.m. so that the velocity of the wires was 7.60 m/s. This reduced the effective turbulence intensity, $u_{rms}/(U+U_p)$, to less than 12% at all radial locations.

The hot-wire signal was transmitted from the probes to the anemometers using low-noise slip-rings. The slip-rings were enclosed in a grounded aluminium housing in order to avoid stray electromagnetic noise. The coaxial cables connecting the slip-rings to the anemometers were also shielded. The noise due to the slip-rings was estimated to be of the order of 1 mV. Both the original velocity signal and its time derivative were recorded for each of the wires.

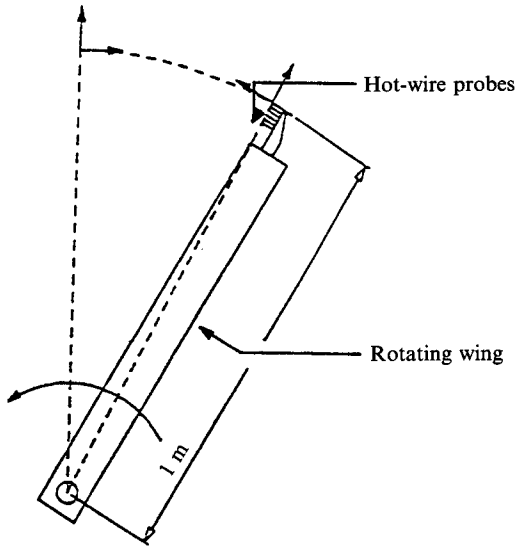

FIGURE 4. Flying hot-wire apparatus.

The data were collected only when the probe was parallel to the axis of the jet. This was accomplished by using an encoder pulse that triggered the A/D converter to collect the data. The short charging time of the sample and hold of the A/D (nanoseconds) ensured that the measurement was effectively taken at a point. One data sample was collected for each revolution, and 4800 samples were taken at each radial position.

Effects of the wing on the flow were carefully studied. The wing has a low coefficient of drag, C_d, of 0.0045 and a Reynolds number of 1700 at 1 m/s. The large-scale characteristics of the flow in the vicinity of the measuring point were observed with smoke wires to ensure that there were minimal amounts of flow disturbances on the jet as the wires rotated through it. This observation was consistent with measurements from a stationary hot-wire made while the ring was rotating nearby. These were indistinguishable from those made without the wing, indicating that whatever disturbances resulted from the wing were convected away from the measuring location.

2.5. *The burst-mode laser Doppler anemometer (LDA)*

The LDA hardware consisted of a two-colour Argon ion model 165 laser system used in combination with Dantec's 55X modular optics and a folded bench. The optics were configured in a back-scatter mode using variable frequency shift. Processing hardware consisted of two modified 55L90a counters, the 55N10 frequency shift unit, and the 57G20 buffer interface to transfer the digital output of the counters to the PDP 11/84. The buffer interface was also fitted with a 57G149 coincidence filter board to ensure simultaneous realizations from both channels.

The counter had been updated by Dantec to include a 10 bit burst time. In order to avoid problems arising from fringe count overflow at the jet's outer edges, the fringe count register was also specially modified by Dantec to a 10 bit register, and to reset when the register was full. (Note that the standard 55L90a counter contains only an 8 bit fringe count register which simply recycles when overflow occurs, thereby introducing major errors in the residence time computation. This probably accounts for many of the problems reported using burst-mode LDA with residence time weighting.) The optics for the two-channel measurements were rotated by 45° so that both channels detected the same mean velocity. With a front lens of focal length 0.6 m

and a 17.8 mm beam separation, the calibration constant for the optics was approximately 17 m/s per MHz. The bandwidth of the filters in the counter was 2 MHz, therefore the frequency shift was chosen to place the mean detected frequency at 1 MHz. Thus, at a position 70 diameters downstream of the jet exit where the r.m.s. velocity at the centreline was 1.4 m/s, the hardware was capable of measurements over a range of 12 standard deviations about the mean velocity. Note that the frequency shift was sufficient to eliminate angle bias (Buchhave 1976; Buchhave, George & Lumley 1979), but not large enough to introduce significant quantization errors (Capp 1983; George 1988).

The data were processed using the residence time weighting technique discussed in detail by Buchhave *et al.* (1979) and George (1988). In brief, all measured moments are weighted by the measured residence times, Δt_j, of the individual scattering particles. Thus the mean is given by

$$\bar{U} = \frac{\sum_{j=1}^{N} (u_{pj})\,\Delta t_j}{\sum_{j=1}^{N} \Delta t_j}, \tag{2.3}$$

and the nth central moment by

$$\overline{u^n} = \frac{\sum_{j=1}^{N} (u_{pj} - U)^n\,\Delta t_j}{\sum_{j=1}^{N} \Delta t_j}, \tag{2.4}$$

where u_{pj} is the velocity of the jth particle, Δt_j is its residence time, and N is total number of particles measured. Both u_{pj} and Δt_j can be determined from the Doppler frequency and fringe count measurements provided on the I/O-2 channel of the modified 55L90a counter. Similar expressions were used for the mixed moments, e.g.

$$\overline{u^m v^n} = \frac{\sum_{j=1}^{N} (u_{pj} - U)^m (v_{pj} - V)^n\,\Delta t_j}{\sum_{j=1}^{N} \Delta t_j}. \tag{2.5}$$

The advantage of the residence time weighting technique is that it avoids most of the sources of bias present in alternative processing techniques, assuming, of course, that additional errors are not introduced by the kind of hardware deficiencies mentioned above (cf. George 1988).

In addition to the two-channel LDA measurements, single-component LDA readings of the axial velocity profile were taken to verify that the coincidence filter board was not biasing the signal. The coincidence filter itself was set to accept data only when the data-ready pulses from both counters were within about 20 % of the average of the two residence times. This introduced a very stringent criterion for rejecting spurious data from either counter, and reduced the effective scattering volume.

The sampling rate of the LDA system, unlike the hot wires, is not fixed, but fluctuates in time and is strongly correlated with the local flow field. To avoid the problem of bias, all laser data was processed using residence time weighting and all data records were taken for a fixed time (as opposed to the more common fixed number of particles). In order to achieve statistical convergence, data was sampled until both a record length of 500 seconds had passed and at least 4500 samples were taken. The

signal-to-noise ratio of the Doppler signal was good, as indicated by the strong correlation between the residence times of different channels (0.85 typically) and between residence time and velocity of the same channel (-0.65 typically).

In spite of the large record sizes, there is still considerably more scatter in the LDA results (typically 5%) than in the hot-wire measurements. Capp (1983) and George (1988) have carefully considered all known sources of random counter errors and concluded that the largest by far is that associated with the fringe count register used to calculate the residence time. For these experiments the r.m.s. value of this error is estimated to be about 2%. This is substantially less than might be inferred from the 0.85 correlation between different channels and indicates that there may be other contributors to this error than those included in the analysis. On the other hand, the random errors present in the measurements may simply be a reflection of the difficulty in maintaining a stable flow for the long periods of time required for the LDA measurements. Since the traverses moved randomly from one radial position to another, any shift in the flow would show up as a random error instead of as a trend. It should be noted, however, that no such drift was apparent in the hot-wire experiments.

The flow was seeded using glycerin smoke (during the LDA measurements only). An estimation of the particle response time (4 μs) shows it to be smaller than the Kolmogorov microtime scale (1 ms) estimated at 70 diameters (see Capp 1983) so that the particle and fluid velocities are identical. Statistically uniform spatial seeding is needed for the computation of bias-free LDA counter measurements in order to uncouple the particle arrival statistics from the flow which transports them (see Buchhave *et al.* 1979; George 1988). This was accomplished by filling the room with smoke prior to the test and using the blower to distribute the particles. The source was then turned off during the test. Even though some seed was probably lost as the air passed through the wire mesh and honeycomb of the jet, at seventy diameters the entrained volume of fluid is an order of magnitude greater than the volume flux at the source so that the effect on the measurements was minimal. That there was little measurable difference in seeding concentration between the jet and its surrounding environment was confirmed by using the average residence time of the particles to infer the concentration (Capp 1983). Thus while the concentration of particles diminished slowly during the test, their distribution remained nearly spatially uniform.

2.6. *Experimental procedure*

First, the characteristics of the jet exit were measured using a single-wire probe. The next step consisted of the alignment of the traversing system with the jet's central axis. The final contraction of the jet was machined from a 4 in. Plexiglas block into which holes were drilled parallel to the jet axis to provide targets for a laser beam to enable an initial rough alignment. The final traverser alignment and verification of flow symmetry was based on velocity contours from 30 to 100 diameters downstream of the jet exit measured using single stationary wire probes. Figure 5 shows a sample of such a plot. With the centreline established, the centreline velocity decay rate was measured and the virtual origin determined. It was desired to record profiles as close to the jet exit as possible in order to maximize the magnitude of the measured velocities and to minimize the effect of the LDA optics on the jet entrainment field. Data from the contour plots was analysed to confirm that the profiles $(U, \overline{u^2}, \overline{u^3}, \overline{u^4})$ displayed self-similar behaviour at both 70 and 100 diameters downstream from the virtual origin. The detailed profiles presented later were taken at a position of 70 diameters downstream from the origin and spanned a range of $-0.16 < \eta < 0.16$. Axial velocity

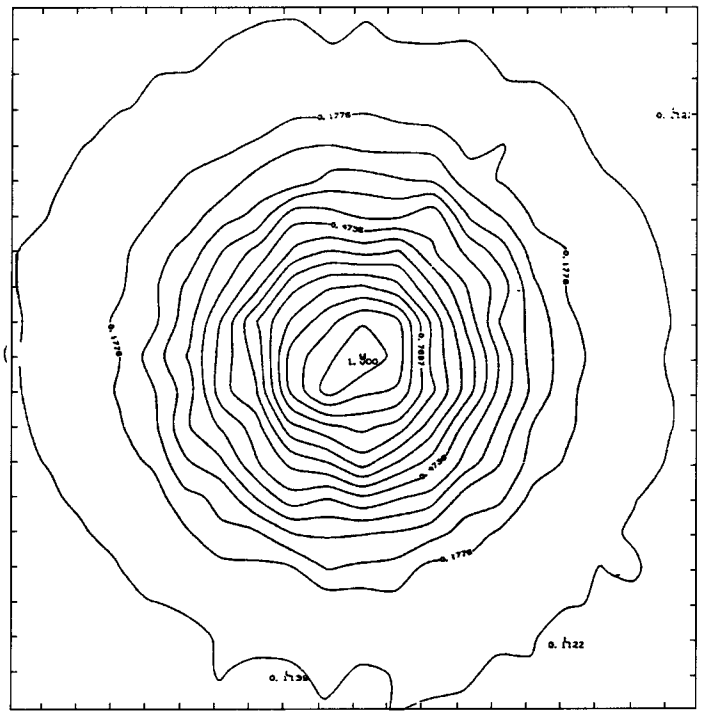

FIGURE 5. Constant axial velocity contours of the jet flow field.

values for the single and cross-wire probes differed by no more than a few per cent across the profile.

Limitations of the laser's traversing system permitted only the axial and radial components of velocity to be measured in this experiment. However, data on the axial and azimuthal components taken during an earlier experiment by Capp (1983) are also presented to further detail the behaviour of the flow field. Thus, only the terms involving cross-correlations between radial and azimuthal components of velocity (e.g. $\overline{vw^2}$) are absent in the FHW and LDA data presented in this paper. Note that the earlier experiment was conducted in a smaller, irregularly shaped enclosure of varying width. The width between 70 and 100 diameters was roughly 14 ft and had a height of only 8 ft. Details of this smaller facility can be found in Capp (1983). Profiles of the axial velocity and its higher moments for both sets of LDA data were consistent with each other and with the FHW data.

In the measurements presented below, the following form is fitted using the method of least squares to all measured profiles:

$$p(\eta) = [C_0 + C_1\eta + C_2\eta^2 + C_3\eta^3 + \ldots + C_n\eta^n]\exp(-A\eta^2). \tag{2.6}$$

The function was taken to be either odd (e.g. $\overline{uv}$) or even (e.g. $\overline{u^2}$) and the appropriate coefficients set to zero. While the polynomial multiplying the exponential allows for an excellent fit over the range in which data were taken ($\eta \leqslant 0.2$), care must be used in applying these fits beyond this range as unphysical sign changes can be encountered. For both the hot-wire and the LDA data of this experiment, the values of these coefficients and the value for the constant in the exponent, A, are listed in tables 4 and 5. The final differential and integral momentum balances for the jet which are presented below are carried out using these fitted functions. Note that no fit is provided for the FHW data since they are in very close agreement with the LDA data.

3. The experimental results

3.1. *The centreline velocity variation and mean velocity profile*

For a self-preserving jet, the centreline velocity is given by

$$U_c = BM_0^{\frac{1}{2}}/(x-x_0), \tag{3.1}$$

where B is a constant and x_0 represents a virtual origin. (Note that both x_0 and B may depend on the exit conditions, George 1989.) From (2.2), this can be written for a top-hat jet as

$$\frac{U_0}{U_c} = \frac{1}{B_u}\left[\frac{x}{D} - \frac{x_0}{D}\right], \tag{3.2}$$

where the constants are related by

$$B_u = \tfrac{1}{2}\pi^{\frac{1}{2}}B. \tag{3.3}$$

The centreline velocity is plotted as a function of axial location in figures 6 and 7. For both graphs, the vertical scales are normalized and the exit velocity U_0 and the horizontal scales are normalized using the exit diameter D. Since the centreline velocity appears in the denominator of the ordinate, the $1/x$ decay rate is represented as a straight line on the plots. The greater the slope of the line, the smaller the value of B and the higher the decay rate of the centreline velocity. The distance between the origin and the x-intercept of the straight line representing the velocity decay is the virtual origin of the jet, x_0. Note that George (1989) and List (1979) have suggested using scales defined from the rate of mass and momentum addition at the source, m_0 and M_0, respectively, i.e.

$$D_* = m_0/(M_0)^{\frac{1}{2}} \tag{3.4}$$

and

$$U_* = M_0/m_0. \tag{3.5}$$

For a top-hat exit velocity profile (which corresponds closely to this experiment),

$$U_* = U_0, \tag{3.6}$$

$$D_* = 2D/(\pi)^2, \tag{3.7}$$

so that the conversion is straightforward.

The SHW centreline mean velocity measurements of this experiment exhibit a decay constant of $B \simeq 6.7$ or $B_u \simeq 5.9$ and a virtual origin of $x_0 \simeq 2.7$. These values are the same as those measured by Peng (1985) from 30 to 50 diameters in this same facility using single-wire probes and Pitot tubes. There is no evidence that these values vary with distance downstream. These results can be contrasted with those of Wygnanski & Fiedler (1969) for which two different virtual origins and decay rates were used: one for $x/D < 50$ ($x_0 \simeq 3D$ and $B \simeq 6.4$ or $B_u \simeq 5.7$) and the other $x/D > 50$ ($x_0 \simeq 7D$ and $B \simeq 5.6$ or $B_u \simeq 5.0$). Although Wygnanski & Fiedler were unable to identify a consistent centreline decay rate between 20 and 100 diameters, they did note that mean velocity profiles collapsed over this range. They concluded that, 'The rate of growth of the jet is sensitive to conditions of self-preservation, while the shape of the normalized velocity profile is not'. The slower decay rate ($B \simeq 5.6$) was assumed to be the correct one, since it was based on the data points farthest downstream and believed to have finally reached the state of self-preservation. Centreline velocity values in our facility do not exhibit this difficulty, and are similar in value to the decay rate and virtual origin indicated by the measurements of Wygnanski & Fiedler taken at distances less than 50 diameters downstream from the exit. The centreline velocity measurements of Rodi

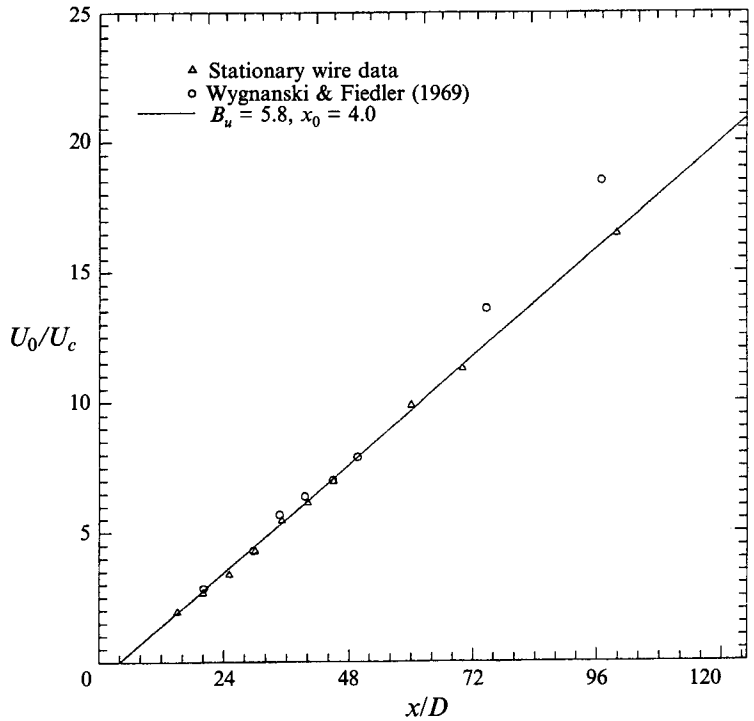

FIGURE 6. Centreline velocity variation with distance from jet, CTA data.

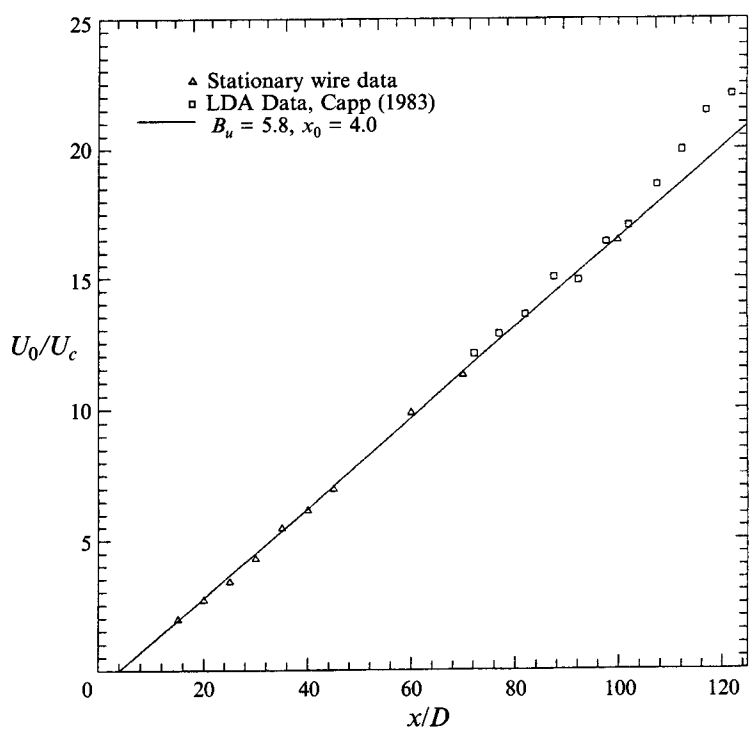

FIGURE 7. Centreline velocity variation with distance from jet, LDA data.

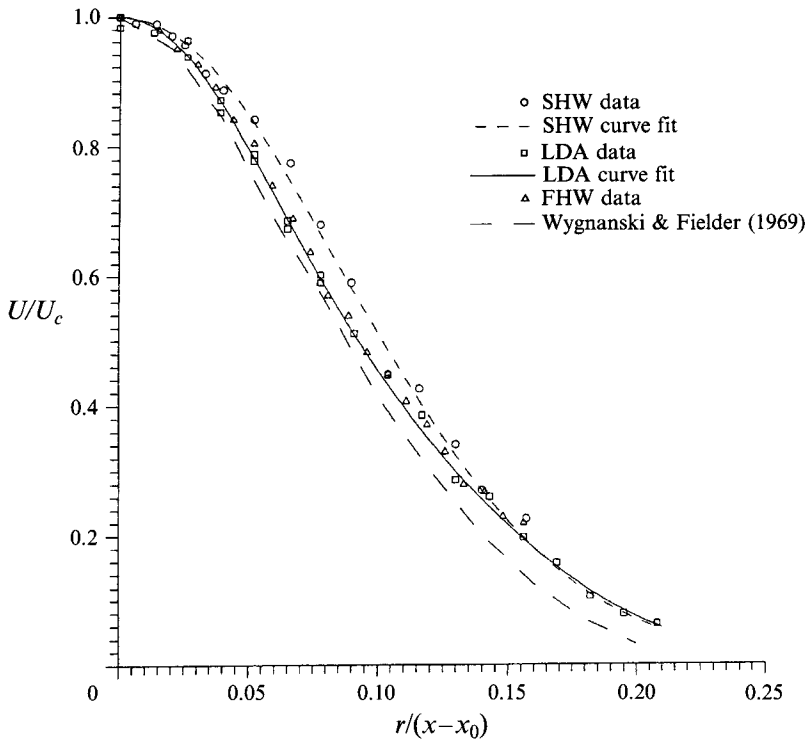

FIGURE 8. Mean velocity profile.

(1975*a*) using hot wires also display a constant decay rate of $B \simeq 6.7$ or $B_u \simeq 5.9$, agreeing with the values of this experiment.

Figure 7 also shows the centreline decay of the same jet in the smaller enclosure as measured with the LDA by Capp (1983). Like the Wygnanski & Fiedler experiment, the centreline mean velocity decay rate of these measurements also fails to stabilize to a constant value. The data break away from the initial line to form a steeper line with a faster decay rate, but at greater distance from the exit than in the Wygnanski & Fiedler data. Thus the virtual origin and the decay rate are dependent upon the data points included in the calculations. The difference between our two experiments can clearly be attributed to the enclosure, the reasons for which will be discussed below. Using only the points within a 100 diameters of the exit, the virtual origin is $x_0 \simeq 4D$ and the decay rate is $B \simeq 6.5$ or $B_u \simeq 5.8$. The slightly lower values of B and B_u observed by the LDA and the slightly higher value of x_0 are consistent with the small but non-negligible effect of the leading cross-flow error terms on the hot wire which can be estimated from table 2 as several per cent. The value of $x_0 = 4D$ will be used for all profiles hereafter.

The mean axial velocity normalized by the centreline velocity, U/U_c, is plotted versus the non-dimensional radial coordinate, $\eta = r/(x-x_0)$, in figure 8. To avoid clutter, the data of Wygnanski & Fiedler has been plotted only as a smooth curve. The mean profiles of the current facility collapse after 30 diameters, but the SHW profile, $\eta_{\frac{1}{2}} \simeq 0.102$ is wider than the FHW or the LDA profiles for which $\eta_{\frac{1}{2}} \simeq 0.094$. This is the expected behaviour, since a binomial expansion of the hot-wire error due to cross-flow effects reveals the leading-error term to be always positive (Beuther *et al.* 1987). Surprisingly, the hot-wire data of Wygnanski & Fiedler, with a half-width of $\eta_{\frac{1}{2}} \simeq$

0.086, falls under all the LDA/FHW and SHW data of the current experiment. The reasons for this will also be discussed below, and be seen to be related to the centreline velocity decay rate discussed above.

3.2. *The momentum integral equation: a first-order evaluation*

An important test of any experimental data is whether it satisfies the equations believed to govern the flow (see George 1990). One of the most important tests of whether the flow being measured is, in fact, a reasonable model of an axisymmetric jet in an infinite environment is whether the velocity moment profiles satisfy the momentum integral given to second order by

$$2\pi \int_0^\infty [U^2 + \overline{u^2} - \tfrac{1}{2}(\overline{v^2} + \overline{w^2})]\, r\, \mathrm{d}r = M_0. \tag{3.8}$$

Note that this is not the momentum flux since it includes the contribution from the streamwise pressure gradient which has been eliminated using the radial momentum equation. Appendix A provides a complete derivation of (3.8).

For a first-order analysis, the integrated momentum balance can be discussed in terms of the contribution due to the mean velocity as fitted by a Gaussian profile which passes through the jet half-width, i.e.

$$U(x, \eta) = \frac{(M_0)^{\frac{1}{2}}}{x} B \exp[-A(\eta/\eta_{\frac{1}{2}})^2], \tag{3.9}$$

where $A = -\ln(0.5) = 0.693$.

Substituting this form into the expression for the contribution of the mean velocity to the momentum integral of (3.8) and ignoring the second-order terms yields

$$\frac{M}{M_0} = 2\pi \int_0^\infty \left[\frac{U}{U_c}\right]^2 (\eta)\, \eta\, \mathrm{d}\eta = \frac{\pi}{2A} (\eta_{\frac{1}{2}} B)^2 = 2.27(\eta_{\frac{1}{2}} B)^2. \tag{3.10}$$

The momentum balance is then only a function of the centreline decay constant, B, and the half-width, $\eta_{\frac{1}{2}}$. Using values of $\eta_{\frac{1}{2}}$ and B from the current investigation, the first-order contribution to the momentum integral is 106% and 85% of the source momentum for the SHW and LDA/FHW data respectively. This can be compared to the value of only 69% obtained from the Wygnanski–Fiedler data (based on their half-width of 0.086 and the early centreline decay constant $B \simeq 6.4$). Thus, a significant portion of the source momentum in their experiment is missing. The situation worsens as one moves downstream since the increase in the slope of the curve describing Wygnanski & Fiedler's data for $x/d > 50$ results in a decrease of B to 5.6 so that only 53% of the momentum is accounted for by the mean flow. Because the momentum flux as expressed by (3.10) is proportional to B^2 (recall the profile is self-similar so that $\eta_{\frac{1}{2}}$ does not change), a decrease in the centreline decay rate produces a significant decrease in the momentum accounted for by the mean profile. It is clear that such a drastic shift in the flow momentum is unlikely, nor can it be accounted for by considering the second-order terms (as shown below).

Why then do the values obtained in the experiments reported here differ so markedly from those of Wygnanski & Fiedler? The answer is to be found in the experimental facilities and not in the measurement techniques and calibration methods. The similarity between the changing slope of the centreline decay in their facility and the earlier data of Capp (1983) measured in an air-tight enclosure is striking. For the case of Capp's data it is obvious the flow is not an ideal jet (that is, a jet in an infinite

environment), but is instead a confined jet in a finite environment. For such flows, conservation of mass demands that a return flow be set up around the outer edges of the facility. Since the mass flux of the jet is increasing with downstream position, the return flow must also increase in magnitude with downstream position. The deceleration of the return flow is accomplished by a favourable pressure gradient ($dP_\infty/dx > 0$), so that P_∞ is not constant but is a function of axial position and increases with increasing x. It must be remembered that even though the magnitudes of U_∞ and dP_∞/dx are small, their effects on the momentum balance when integrated over a large area are significant. Because of this integration, it cannot be concluded that if the magnitude of the return flow, U_∞, is much smaller than the centreline velocity, U_c, that the flow is guaranteed to behave as a jet in an infinite environment. Additional discussion of this phenomenon can be found in Capp (1983) and in Appendix B (see also George 1990).

As is clear from Appendix B, the effect of the return flow is to steal momentum from the jet so that the experiment no longer simulates a jet in a free environment, but rather one in a box.† Even though the facilities of Wygnanski & Fiedler were surrounded by a wire enclosure, the behaviour pattern of the centreline decay rate indicates that the jet's behaviour was strongly influenced by backflow. The success of the measurements of the current experiment in conserving momentum can thus be attributed to the increased size of the facility. Now that both the error in these earlier data and its source have been identified, the remainder of this paper will focus on the results and the validation of the data from the current investigation.

3.3. *The jet entrainment*

The mass per unit length entrained by flow, ρE, can be obtained by integrating the continuity equation with the result that

$$E = \lim_{r\to\infty}(-2\pi r V) = \frac{\mathrm{d}}{\mathrm{d}x}\left[2\pi\int_0^\infty Ur\,\mathrm{d}r\right] = 2\pi B(M_0)^{\frac{1}{2}}\int_0^\infty\left[\frac{U}{U_c}\right]\eta\,\mathrm{d}\eta. \tag{3.11}$$

Using the curve-fit for the mean velocity (LDA) from table 4 yields the value of the integral to be about 0.14. Note that the curve is well-behaved, even for values of $\eta > 0.2$; moreover the integral has obtained more than 90% of its value by $\eta = 0.2$. Therefore considerable confidence can be placed in this estimate.

Morton, Taylor & Turner (1956) define an entrainment coefficient by

$$\alpha = \frac{E'}{2bW}, \tag{3.12}$$

where E', b, and W are the equivalent top-hat parameters defined by

$$b^2W = 2\int_0^\infty Ur\,\mathrm{d}r, \tag{3.13}$$

$$b^2W^2 = 2\int_0^\infty U^2r\,\mathrm{d}r, \tag{3.14}$$

$$E' = \frac{\mathrm{d}}{\mathrm{d}x}\left(2\int_0^\infty Ur\,\mathrm{d}r\right). \tag{3.15}$$

† Similar considerations have long been known to the ventilation community (Baturin 1972). The authors are grateful to Professor T. Malmstrom KTH, Stockholm for making us aware of this literature.

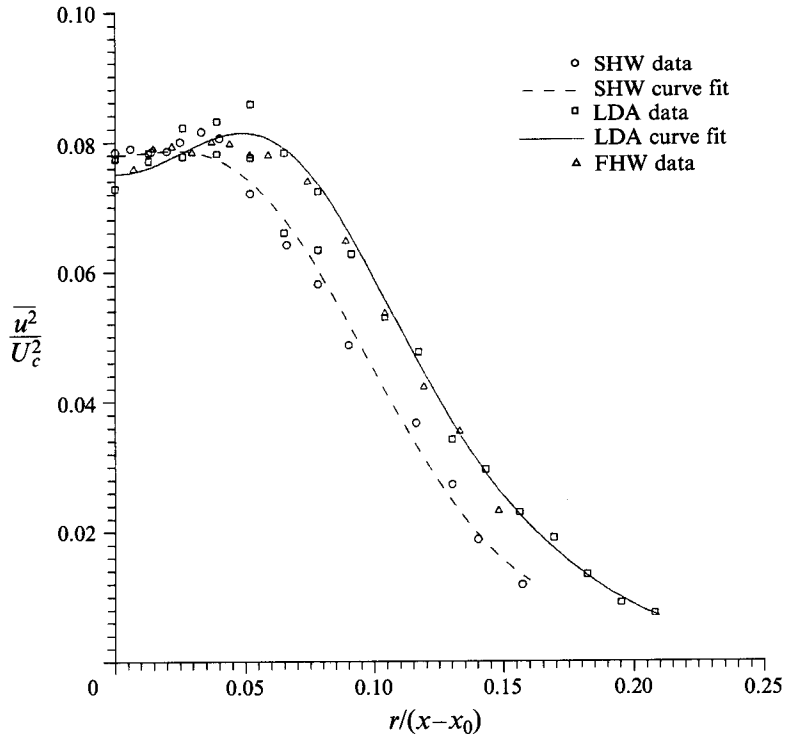

FIGURE 9. Axial component of turbulence kinetic energy, $\overline{u^2}/U_c^2$.

It is easy to show that for the self-preserving jet,

$$b = I_1 x/(I_2)^{\frac{1}{2}}, \tag{3.16}$$

$$W = (I_2/I_1)\, B(M_0)^{\frac{1}{2}}/x, \tag{3.17}$$

$$E_2 = I_1 B(M_0)^{\frac{1}{2}}, \tag{3.18}$$

where

$$I_1 = 2\int_0^\infty \frac{U}{U_c}\eta \,\mathrm{d}\eta, \tag{3.19}$$

$$I_2 = 2\int_0^\infty \left(\frac{U}{U_c}\right)^2 \eta \,\mathrm{d}\eta. \tag{3.20}$$

It follows that

$$\alpha = I_1/2(I_2)^{\frac{1}{2}}. \tag{3.21}$$

For the LDA/FHW data of the present experiment, $I_1 \cong 0.014$ and $I_2 \simeq 0.0066$ so that $\alpha \simeq 0.081$. This is in striking agreement with the value of 0.08 obtained by Ricou & Spalding (1961) by direct measurement, and adds to the credibility of both experiments. For the SHW mean velocity profile, on the other hand, $I_1 \simeq 0.015$ and $I_2 \simeq 0.0077$ corresponding to $\alpha_{HW} = 0.097$. This is considerably higher than earlier estimates based on hot-wire measurements, and a consequence of the somewhat broader profiles resulting from the rectification and cross-flow errors on the wire. Note that the lower values from earlier experiment must be regarded as unreliable because the flows were not really reasonable models of jets in an infinite environment. Also it should be remarked that in view of the new understanding of self-preservation (George

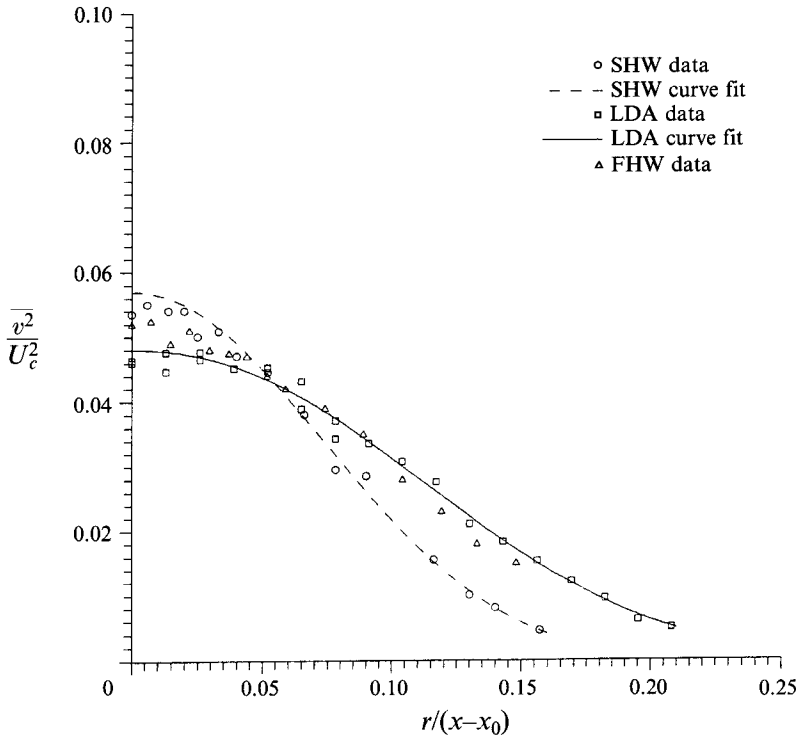

FIGURE 10. Radial component of turbulence kinetic energy, $\overline{v^2}/U_c^2$.

1989, and Appendix C) there is no reason to regard these spreading and entrainment rates as universally characterizing all jets. Rather they should be expected to vary (at least weakly) with exit conditions and Reynolds number.

3.4. *The second moments of velocity*

The Reynolds stresses in $\overline{u^2}$, $\overline{v^2}$, $\overline{w^2}$ and $\overline{uv}$, are plotted in figures 9–12, respectively. In all plots, the Reynolds stresses are non-dimensionalized by the square of the centreline velocity as seen by the respective measuring hardware. The LDA/FHW measurements were normalized by a centreline velocity of 4.82 m/s. The normalized centreline values for the normal stresses $\overline{u^2}$, $\overline{v^2}$ and $\overline{w^2}$ measured by the LDA are 0.076, 0.047 and 0.049, respectively. Note that the axisymmetry of the flow requires that $\overline{v^2}$ and $\overline{w^2}$ be equal, a condition nearly satisfied by the data. The SHW measured a centreline value for $\overline{u^2}/U_c^2$ of 0.078, only 4% higher than the LDA. If, however, we recall that the SHW has also overestimated U_c, the actual error in the direct measurement of $\overline{u^2}$ is closer to 7.5%. Unless specifically noted, all data comparisons in the following discussion are between values of the normalized data, so that a comparison of the raw data values would exhibit an even greater disagreement. The normalized SHW centreline values for the radial and azimuthal normal stresses have nearly the same value of (0.005 *vs.* 0.058) and significantly overshoot the LDA values. Inexplicably, so do the FHW data, but only near the axis. Elsewhere, and for all other moments the FHW and LDA data are in virtual agreement.

The profile of the axial normal stress measured with the SHW fails to detect the distinct off-axis peak detected by the LDA/FHW. This peak is consistent with model calculations and is due to the strong off-axis peak in the production of turbulence

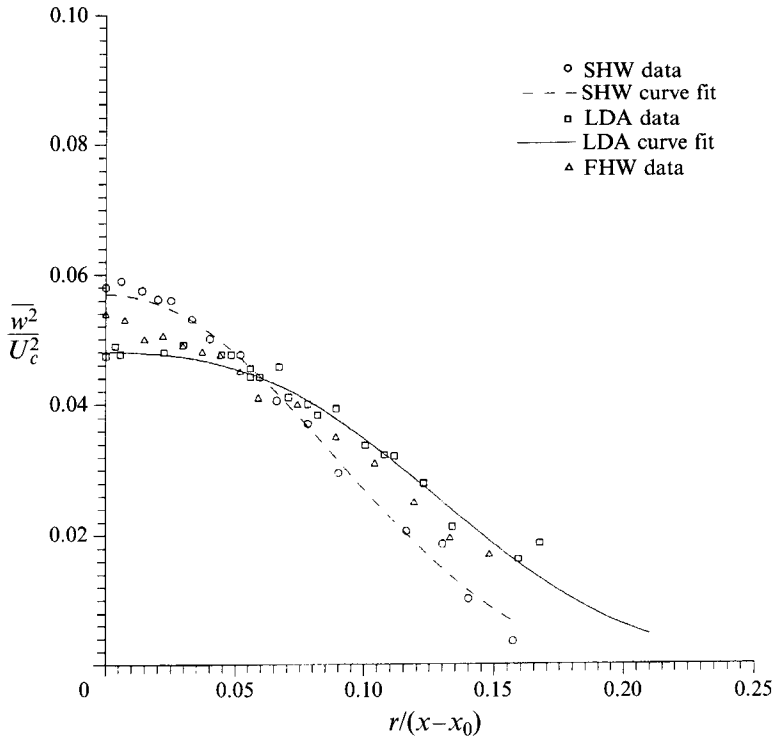

FIGURE 11. Azimuthal component of turbulence kinetic energy, $\overline{w^2}/U_c^2$.

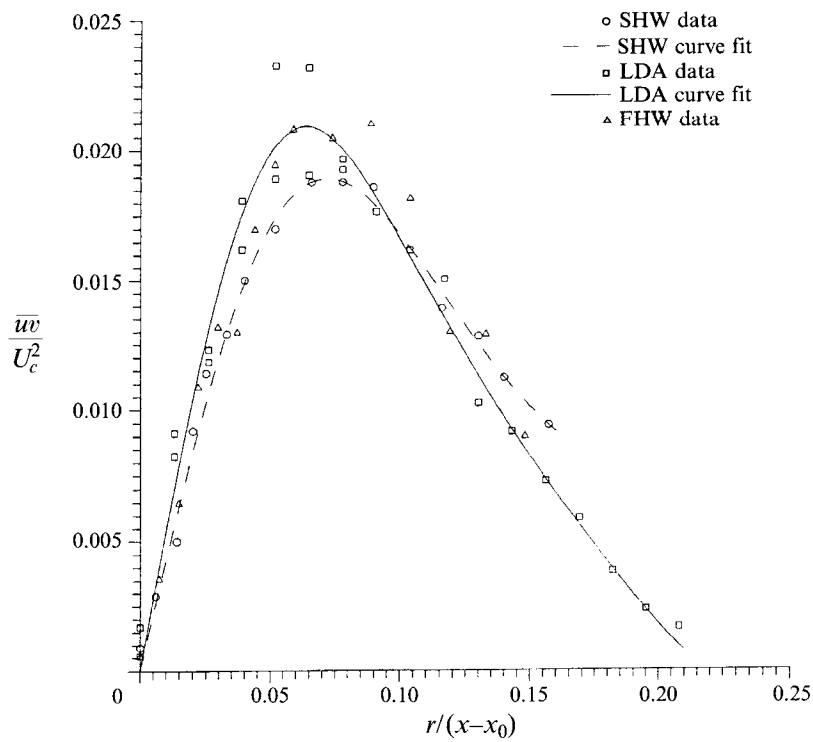

FIGURE 12. Turbulence shear stress $\overline{uv}/U_c^2$.

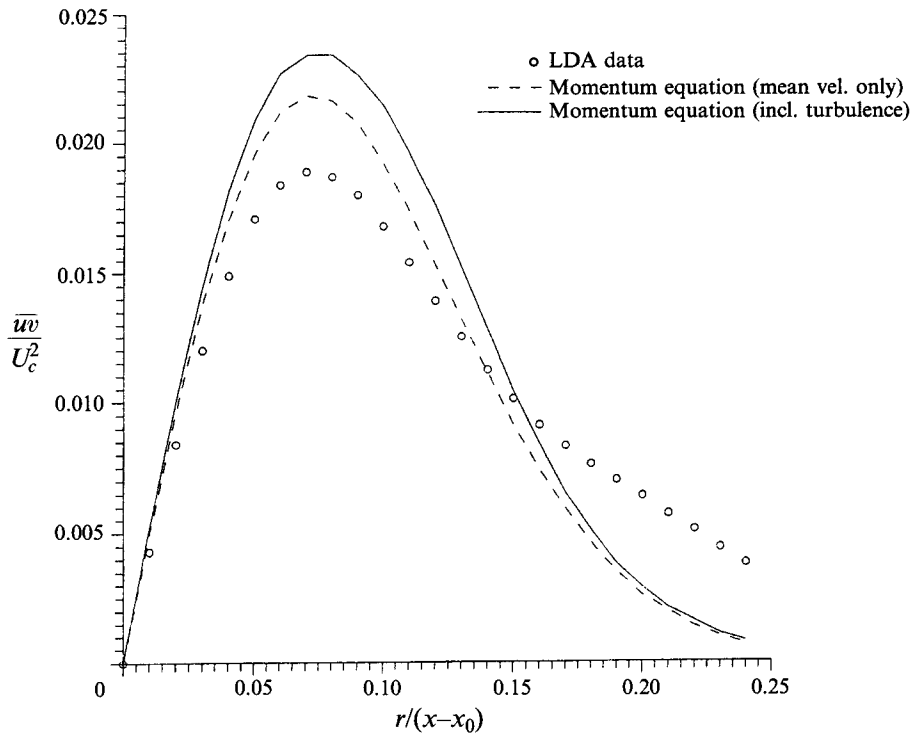

FIGURE 13. Turbulence shear stress calculated from (3.22) using SHW data.

energy by the Reynolds stress working against the mean shear. This peak in $\overline{u^2}$ occurs at a value of $\eta \simeq 0.04$. The largest discrepancies occur off-axis at higher turbulence intensities. Here the SHW profiles decrease much more rapidly with radius and pass under the LDA/FHW curves. At a value of $\eta \simeq 0.1$ (near the jet half-width) the local turbulence intensity, u'/U, is approximately 55% and the normalized SHW values are roughly 25% less than those measured by the LDA/FHW. For all the normal stresses the relative error continues to grow with increasing radial coordinate. The disagreement between the SHW and LDA profiles is much more pronounced in the second-order moments than in the mean velocity profile, but the latter are virtually identical to the FHW data.

The differences between SHW and LDA/FHW second moment data are consistent with the equations in table 2 for the cross-flow errors (except for the discrepancy near the axis). For the second-order moments, these depend on the third-order moments, and are therefore only one level higher than the measured quantity. Thus the SHW second moments are subject to greater contamination than the estimates for the mean values. It might be tempting to try to use the expansions of table 2 to correct the second-order measurements; however, even though one might model the higher-order even terms using a Gaussian approximation (e.g. Tutu & Chevray 1975), no convenient approximation is apparent for the third-order moments. Also, flow reversal and prong interference errors are not accounted for in these analyses and the higher-order terms have been observed to drop off very slowly. As a consequence, it is not generally possible to correct the hot-wire measurements.

The consistency of the data of the current experiment can be evaluated by substituting the first and second moments into the differential equations of motion for

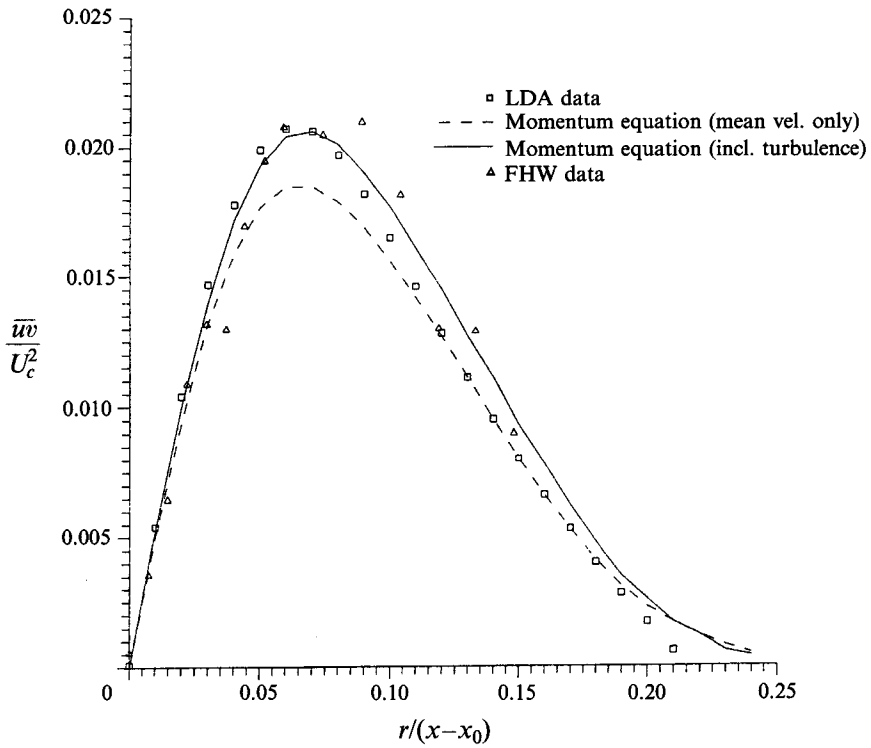

FIGURE 14. Turbulence shear stress calculated from (3.22) using LDA data.

a free jet. By using the radial momentum equation to eliminate the pressure, neglecting terms above second order and integrating with respect to radius, the streamwise momentum equation can be solved for the Reynolds stress to yield (Appendix A, equation (A 3)),

$$\frac{\overline{uv}}{U_c^2} = \frac{1}{\eta}\left[\frac{U}{U_c}\right]\int_0^{\eta}\left[\frac{U}{U_c}\right]\bar{\eta}\,\mathrm{d}\bar{\eta} + \eta\left(\frac{\overline{u^2}-\overline{v^2}}{U_c^2}\right) + \eta\int_{\eta}^{\infty}\frac{\overline{v^2}-\overline{w^2}}{\bar{\eta}U_c^2}\mathrm{d}\bar{\eta}. \tag{3.22}$$

If the data is consistent with the differential equations of motion, the Reynolds stress should be successfully predicted by the measured values of the terms on the right-hand side. The results of this integration are shown in figures 13 and 14. Each plot consists of the measured data points, a dashed line for a simplified prediction of $\overline{uv}$ based on the mean velocity alone (first term on the right-hand side of the above equation) and a solid line calculated using the full form of (3.22).

The SHW results are documented in figure 13. For the simplified estimate, the peak value of the Reynolds stress is overestimated while towards the outer edge ($\eta > 0.15$) it is too low. When the second-order terms are inserted, the predicted value of $\overline{uv}$ increases everywhere across the jet. The prediction near the peak value becomes worse while the accuracy at the outer edges is not significantly improved. Evidently, the SHW data does not satisfy the equations of motion nor should it be expected to do so because of the cross-flow and rectification errors.

The LDA/FHW data of figure 14 exhibits the expected behaviour. Here, unlike the SHW data, the first-order prediction underestimates the Reynolds stress, while the correction due to the second-order terms brings the predicted values up to the

	U^2	$\overline{u^2}$	$\overline{v^2}$	$\overline{w^2}$	Total (equation (3.9))
LDA	0.87	0.24	0.13	0.15	0.97
SHW	0.99	0.14	0.07	0.05	1.07

TABLE 3. Momentum integral results, equation (3.8)

	Probe type	C_0	C_2	C_4	C_6	A
$\bar{U}$	L	1.000	1.212×10^{1}	2.815×10^{3}	—	111
	HW	1.00	-1.925	—	—	63
$\overline{u^2}$	L	7.648×10^{-2}	1.729×10^{1}	-4.845×10^{2}	5.864×10^{4}	156
	HW	7.778×10^{-2}	2.79×10^{1}	-2.02×10^{3}	4.30×10^{5}	257
$\overline{v^2}$	L	4.723×10^{-2}	2.222	5.174×10^{-1}	—	79
	HW	5.457×10^{-2}	0.355	-4.298×10^{1}	—	89
$\overline{w^2}$	L	4.900×10^{-2}	2.316	5.745×10^{-1}	—	73
	HW	5.78×10^{-2}	-1.71	2.73×10^{-1}	—	42
$\overline{u^3}$	L	2.139×10^{-3}	2.398	-1.551	1.889×10^{3}	134
	HW	2.14×10^{-3}	1.008	-4.763×10^{1}	5.54×10^{2}	75
$\overline{uv^2}$	L	-1.252×10^{-3}	8.746×10^{-1}	-7.08×10^{-1}	8.995×10^{2}	135
	HW	2.20×10^{-3}	1.237	-5.888×10^{1}	7.81×10^{2}	95
$\overline{uw^2}$	L	-1.220×10^{-3}	-1.645×10^{-1}	2.558×10^{2}	4.238	262
	HW	2.85×10^{-3}	1.04×10^{1}	-9.20×10^{2}	1.98×10^{4}	65

TABLE 4. Curve fits for even functions, $p(\eta) = [C_0 + C_2\eta^2 + \ldots]e^{-A\eta^2}$

	Probe type	C_1	C_3	C_5	C_7	A
$\overline{uv}$	L	5.500×10^{-1}	-2.962×10^{1}	1.282×10^{3}	-1.898×10^{4}	78
	HW	4.375×10^{-1}	-3.931×10^{1}	1.55×10^{2}	1.342×10^{4}	90
$\overline{vu^2}$	L	-3.870×10^{-2}	2.647×10^{1}	-7.988×10^{2}	5.340×10^{4}	195
	HW	3.33×10^{-2}	1.59×10^{1}	-2.87×10^{2}	—	169
$\overline{v^3}$	L	4.870×10^{-2}	3.518×10^{-1}	6.771	-6.250×10^{2}	65
	HW	1.2×10^{-1}	7.27×10^{-1}	2.09×10^{3}	—	246
$\overline{vw^2}$	L	—	—	—	—	—
	HW	3.0×10^{-2}	5.17	-4.83×10^{2}	7.587×10^{3}	100

TABLE 5. Curve fits for odd functions, $p(\eta) = [C_1\eta + C_3\eta^3 + \ldots]e^{-A\eta^2}$

measured profile. Based on these results, it can be concluded that all of the first and second moments measured by the LDA (that is U, $\overline{u^2}$, $\overline{v^2}$, $\overline{w^2}$ and $\overline{uv}$) are compatible with the equations of motion. Similar conclusions can be drawn for the FHW data.

The final verification of the data is evidenced by the full momentum balance of (3.8). This balance is calculated using the fitted equations with form described by (2.6) and coefficients as listed in tables 4 and 5. The integral results are summarized in table 3. The first four columns of table 3 list the contribution from each individual term, while the last column lists the sum total. Because the simple Gaussian form of (3.9)

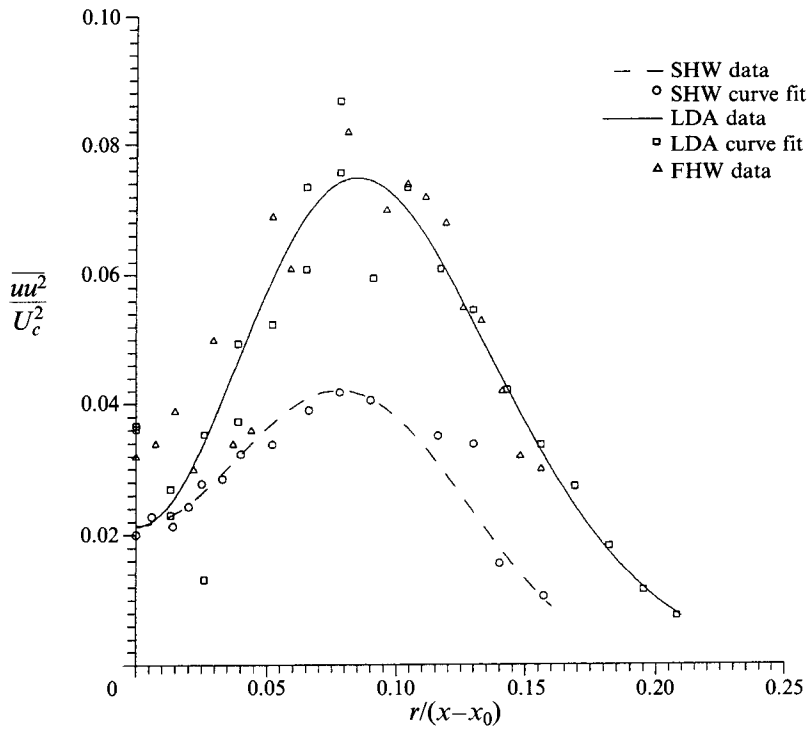

FIGURE 15. Axial flux of $\overline{u^2}, \overline{u^3}$.

underestimates the mean profile at the outer edges, the contribution of the mean velocity to the momentum flux is larger than the values presented in §3.2. The mean velocity accounts for the majority of the momentum flux: 99% for the SHW data and 92% for the LDA/FHW data. The contribution of the axial component of turbulent kinetic energy, $\overline{u^2}$, accounts for an additional 14%/24% in the SHW/LDA balance. The reason for the large difference can be seen easily from figure 9 where the significantly larger off-axis values of $\overline{u^2}$ are magnified by the multiplication by radius in the integrand. Note that the profiles of radial and azimuthal turbulent kinetic energy, $\overline{v^2}$ and $\overline{w^2}$, are nearly equal within each set of measurements so that the contribution due to each term is roughly the same in their respective balances (half of 7%/13% and 5%/15%). Their net contribution is to remove approximately half of the momentum contributed by $\overline{u^2}$. The final totals reveal that the SHW data, as expected, significantly overestimate the momentum flux by 7%, while the LDA data is 3% too low. That the LDA and FHW momentum flux can be conserved with this accuracy must be regarded as gratifying and lends considerable credibility to the experiment, especially considering the scatter within the LDA/FHW data, the possible effect of the small return flow present even with the large enclosure, and the difficulty in integration at the outer edge of the jet (where both the area and the errors in the averaging process become large).

3.5. *The third-order velocity moments*

The major significance of the third-order moments is due to their appearance as transport terms in the mean kinetic energy budget of the turbulent velocity fluctuations. Since it is the gradients of these terms which appear in that energy balance, differences

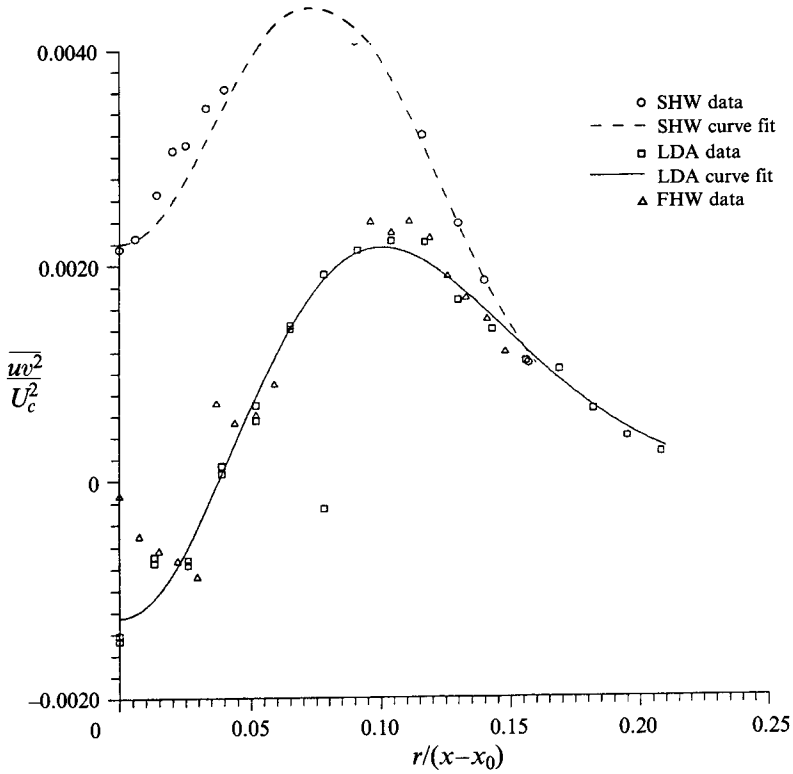

FIGURE 16. Axial flux of $\overline{v^2}, \overline{uv^2}$.

in the slope between the SHW and LDA/FHW results are very important. Unfortunately, it is in the third moments of the velocity field that the largest differences are observed.

The terms for the axial transport of turbulent kinetic energy are plotted in figures 15–17. These figures reveal significant differences in shape, slope and magnitude between the SHW and LDA/FHW axials. All curve fits for these third-order terms are expressed in terms of even powers, ensuring a zero slope at the jet centreline. The functional fit to these profiles are presented in tables 4 and 5. Peak values for these fits along with their locations are presented in this discussion. For both clarity and brevity of presentation, results of the LDA/FHW investigation will be denoted using the subscript L, while the SHW results will be identified using the subscript HW. Since the FHW and LDA results are virtually identical, no distinction is made between them in the discussion.

The transport of axial kinetic energy, $\overline{u^3}$, is presented in figure 15. Away from the centre, the LDA/FHW profile is higher than the SHW profile at all points across the profile, as evidenced by the centreline values of 0.00214_L and 0.00214_{HW} and peak values of 0.00749_L and 0.00420_{HW}. Not that the peak values of both measured profiles occur at the same approximate position, 0.084_L and 0.078_{HW}. Because the peak value of the LDA/FHW data is much higher than that of the SHW, the gradient of the former near the origin ($0.02 < \eta < 0.06$) is approximately twice that of the latter.

The axial transport of the radial component of turbulent kinetic energy, $\overline{uv^2}$, is presented in figure 16. The SHW fails to detect negative values near the origin as reflected in the centreline values of -0.00125_L versus $+0.00220_{HW}$. The LDA/FHW

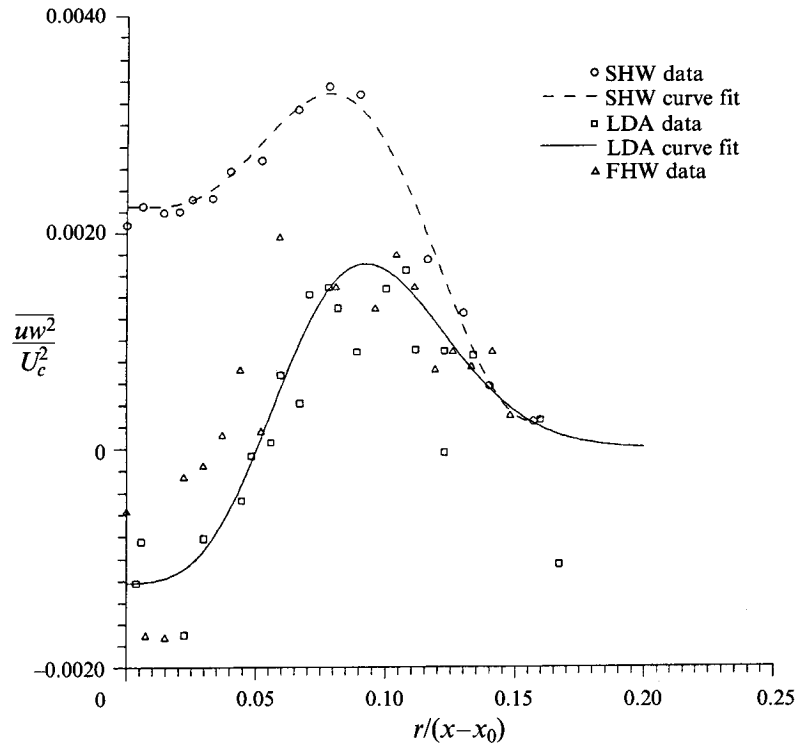

FIGURE 17. Axial flux of $\overline{w^2}, \overline{uw^2}$.

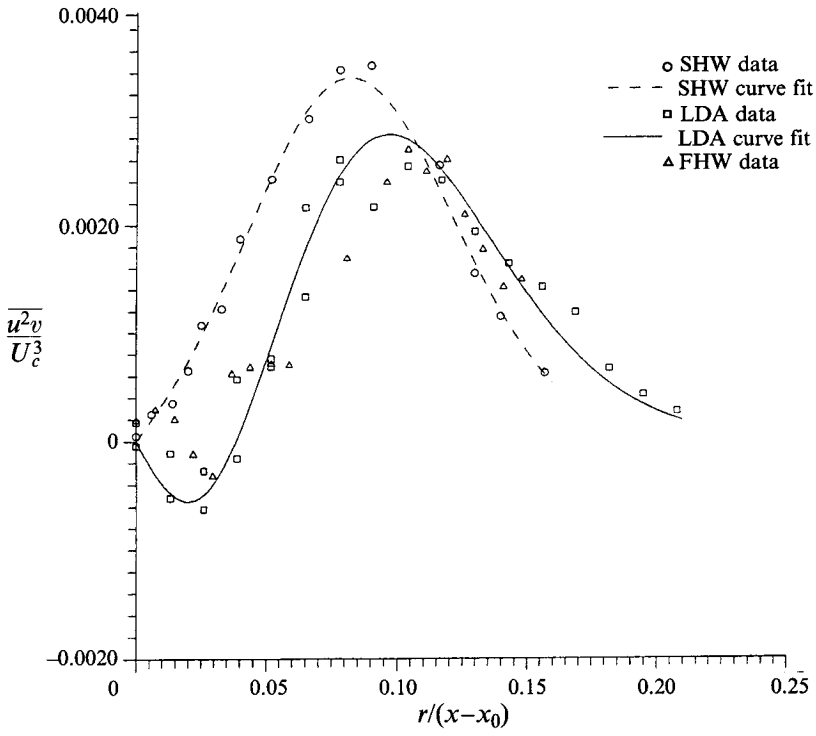

FIGURE 18. Radial flux of $\overline{u^2}, \overline{u^2v}$.

profile crosses the axis at $\eta = 0.037_L$ and increases to a peak value of 0.00216_L versus 0.00436_{HW}. Consequently, the SHW data is significantly higher than the LDA/FHW, except at the outer edges of the jet ($\eta > 0.16$). The peak value for the LDA/FHW profile is farther out, at a radial coordinate of 0.10_L contrasted to 0.073_{HW}. Although gradients near the origin for both sets of data are roughly the same, the differences in the radial location and the magnitude of the maximum value of the profiles results in differences in values of the radial gradients for locations where $\eta > 0.08$.

The remaining axial transport term of azimuthal turbulent kinetic energy, $\overline{uw^2}$, is graphed in figure 17, and is very similar in behaviour to figure 16. As before, the SHW fails to measure negative values near the origin, while the LDA/FHW does not become positive until $\eta = 0.043$. The centreline values of -0.00125_L and $+0.0029_{HW}$ along with the peak values of 0.00123_L and 0.0024_{HW} at 0.097_L and 0.070_{HW}, are roughly the same as those presented in the preceding paragraph for $\overline{uv^2}$. The pattern for the slopes of the profiles is also repeated.

A comparison between the profiles for the axial transport terms indicates that $\overline{u^3}$ is much higher than the other axial transport terms. The ratio of the peak values for the LDA/FHW data are 3.5:1 and 6:1 for $\overline{u^3}:\overline{uv^2}$ and $\overline{u^3}:\overline{uw^2}$, respectively. The peak values for all three profiles occur at the same approximate radial location of $\eta \cong 0.09 \pm 0.01$.

Owing to the limitations of the LDA optical configuration, only two of the three radial transport terms, $\overline{vu^2}$ and $\overline{v^3}$, were measured using both SHW and LDA. The third term $\overline{vw^2}$, was measured using only the SHW. Fitted curves for the radial transport terms are determined using odd powers for the polynomials with zero centreline values. These data are plotted in figures 18–19. Although the plots do not show the large disagreement evidenced in the axial transport terms, the differences are still significant.

The radial transport of axial kinetic energy, $\overline{vu^2}$, is pictured in figure 18. The LDA/FHW profile exhibits a relative minimum ($\overline{vu^2} = -0.000523$ at $\eta = 0.021$) just to the right of the origin. The SHW fails to detect these small negative values. The LDA/FHW values remain below those of the SHW, although the slopes for both curves are approximately equal for $0.02 < \eta < 0.08$. The peak value of the LDA/FHW curve (0.00283_L and 0.00335_{HW}) occurs at a slightly greater radial coordinate than the SHW (0.096_L versus 0.082_{HW}). The SHW profile passes beneath the LDA/FHW at $\eta = 0.108$, shortly after reaching its peak, and then decays at a faster rate.

Figure 19 shows the results for the transport of radial kinetic energy, $\overline{v^3}$. Note that no negative values are found for either curve. The SHW data initially has a steeper slope, and again peaks at a higher value of 0.0037_{HW}. The LDA/FHW maximum of 0.00275_L is once more found at a larger value of η, 0.093_L as opposed to 0.059_{HW}. The SHW profile is narrower, with a steeper gradient at the outer edge ($\eta > 0.06$).

Figure 20 shows the radial transport of $\overline{w^2}$, $\overline{vw^2}$, as measured by the SHW alone. In addition to the problems with rectification and cross-flow, this measurement is also complicated by the need to use two cross-wires in close proximity. The loss of correlation because of the spacing between the probes is believed to be minimal; however, the additional effects due to prong wakes cannot be estimated. In view of the problems with the SHW results for the other third moments and the absence of LDA results, little confidence should be placed in these results, especially away from the axis. Thus, the failure to obtain this moment with the LDA or FHW represents a major shortcoming of this experiment. In the energy balance which follows it will be assessed that $\overline{vw^2} = \overline{v^3}$ in the absence of better information.

In summary, the most striking difference between the SHW and LDA/FHW third moment results is the appearance of the sign reversals near the axis in the latter. These

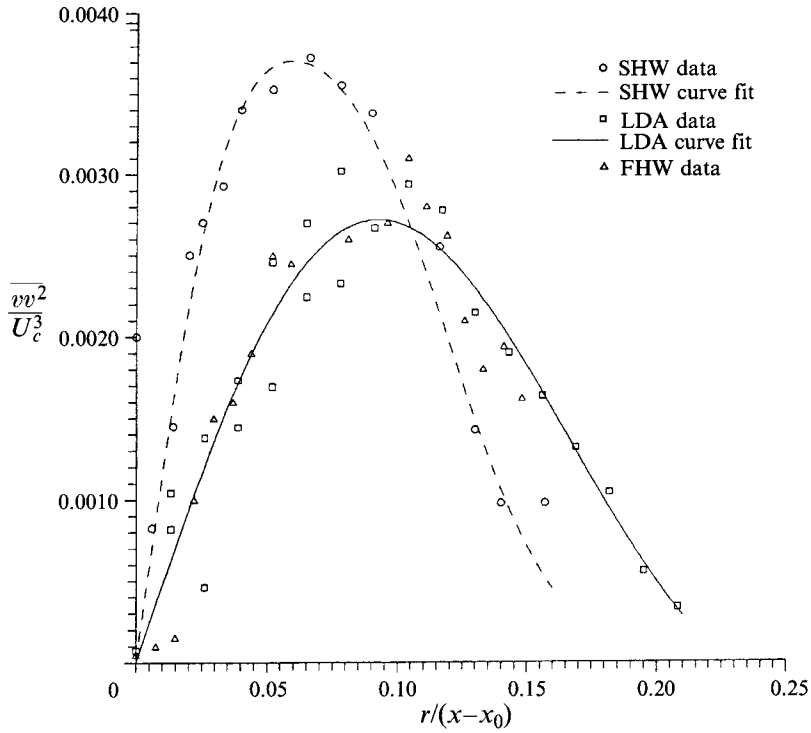

FIGURE 19. Radial flux of $\overline{v^2}, \overline{v^3}$.

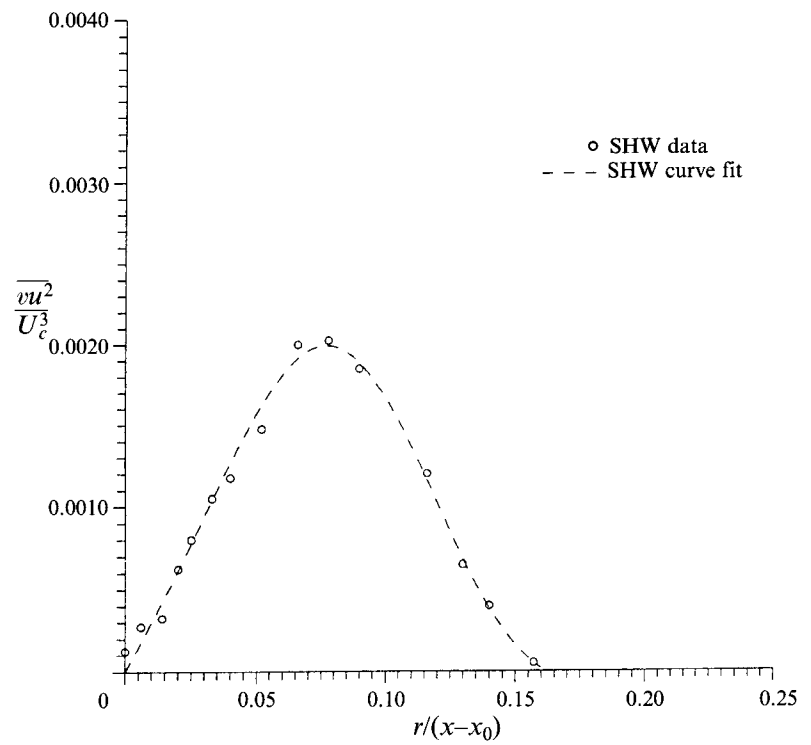

FIGURE 20. Radial flux of $\overline{w^2}, \overline{vw^2}$.

negative regions are consistent with the physics and with most second-order models, and indicate a flux of energy toward the axis and away from the regions of peak production which are off-axis. Their absence in the SHW measurements can be explained by reference to table 2 which shows that the leading cross-flow error terms for the third moments are proportional to the fourth-order moments. Thus, when the third moments are themselves small (e.g. near the axis) the largest contributors to the measured moments are the error terms which are positive. No such simple explanation is possible for the large differences between the SHW and LDA/FHW results away from the core region of the jet since the expansions leading to the equations in table 2 are no longer valid because of the high turbulence intensity. In view of the nature of the error terms and the increasing importance of the higher-order terms with distance from the axis, it would have been surprising if the results were in closer agreement.

4. Inferences from the data

4.1. *Energy balance and dissipation*

If the pressure–velocity correlations and dissipation were known it would be possible to check whether or not the data satisfy the turbulence kinetic energy equation given for this flow by

$$0 = -\left[U\frac{\partial k}{\partial x}+V\frac{\partial k}{\partial r}\right]-\frac{1}{r}\frac{\partial}{\partial r}r\left(\frac{1}{\rho}\overline{pv}+\tfrac{1}{2}\overline{q^2v}-\nu\frac{\partial k}{\partial r}\right)-\frac{\partial}{\partial x}\left(\frac{1}{\rho}\overline{pu}+\tfrac{1}{2}\overline{q^2u}-\nu\frac{\partial k}{\partial x}\right)$$
$$-\left[\overline{uv}\left(\frac{\partial U}{\partial r}+\frac{\partial V}{\partial x}\right)+\overline{u^2}\frac{\partial U}{\partial x}+\overline{v^2}\frac{\partial V}{\partial r}+\frac{V}{r}\overline{w^2}\right]-\epsilon_{hom}. \quad (4.1)$$

The term ϵ_{hom} is defined by

$$\epsilon_{hom} = \nu\overline{(\partial u_i/\partial x_j)^2}, \quad (4.2)$$

which reduces to the actual dissipation, $\epsilon = 2\nu\overline{e_{ij}^2}$ for locally homogeneous flow (see George & Hussein 1991). It is convenient to define a 'transport dissipation' which includes both the homogeneous dissipation and the two pressure–velocity terms, i.e.

$$\epsilon_{tr} = \epsilon_{hom}+\frac{\partial}{\partial x}\left(\frac{1}{\rho}\overline{pu}\right)+\frac{1}{r}\frac{\partial}{\partial r}\left(\frac{r}{\rho}\overline{pv}\right). \quad (4.3)$$

In the present experiment, $\overline{pu}/\rho$ and $\overline{pv}/\rho$ could not be measured directly. Also, the moment $\overline{vw^2}$ was not measured by either the LDA or the FHW, and the SHW results are not deemed to be reliable because of the high turbulence intensity. In the balances computed below, it was assumed that $\overline{vw^2} = \overline{v^3}$. While certainly less satisfactory than direct measurement, the errors introduced by this assumption have been estimated at less than 10% by computing the balance with the $\overline{vw^2}$ term identically zero.

George & Hussein (1991) report several dissipation estimates based on direct measurements of velocity derivatives using the flying hot wires in the same facility under identical operating conditions. Curve fits to these data are provided in table 4. These are shown in figure 21(*a*), along with the transport dissipation calculated using (4.1) and (4.3). Two of the curves shown are based on the assumption of local isotropy using

$$\epsilon_{iso} = 15\nu\overline{\left(\frac{\partial u}{\partial x}\right)^2} = \tfrac{15}{2}\nu\overline{\left(\frac{\partial u}{\partial y}\right)^2}, \quad (4.4)$$

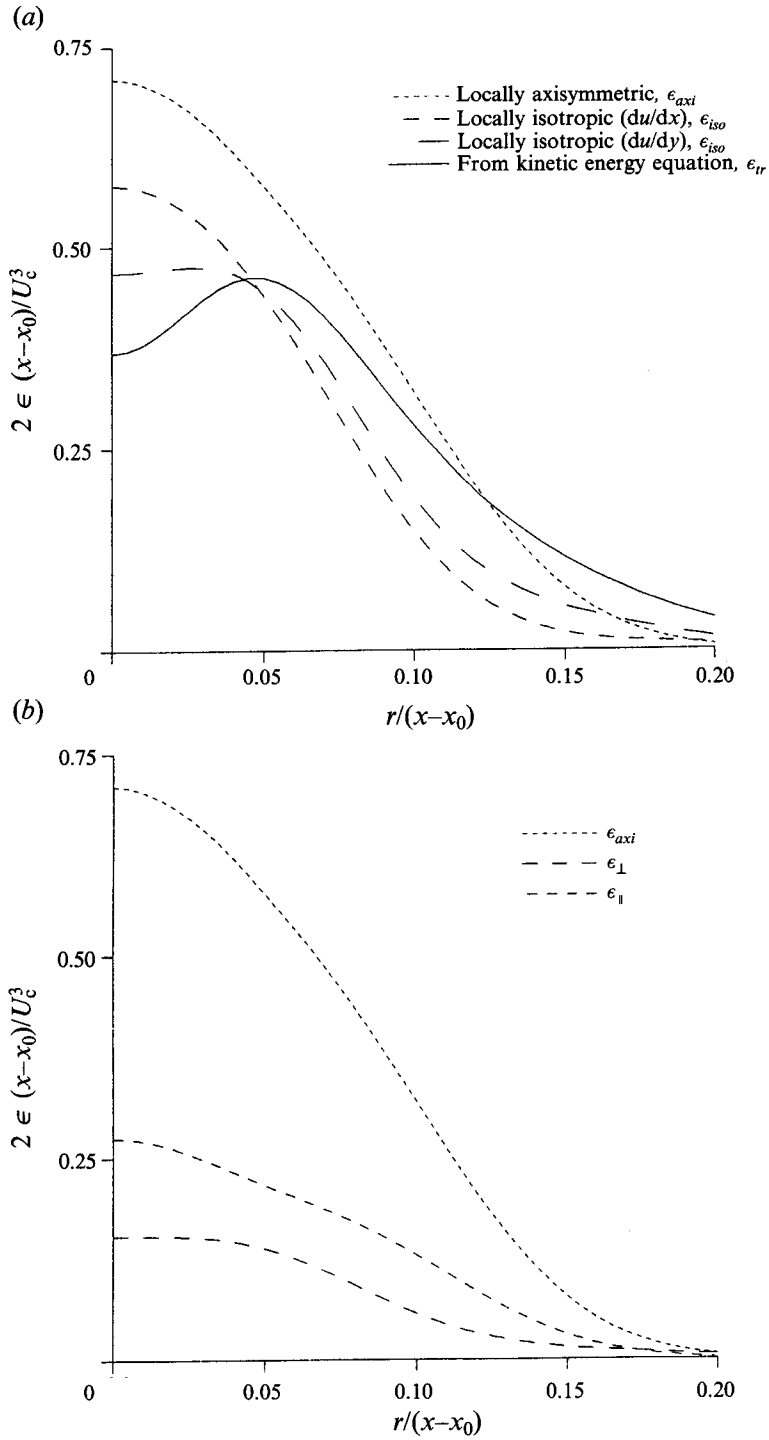

FIGURE 21. (*a*) Dissipation estimates. (*b*) Component dissipations.

	C_0	C_2	C_4	C_6	A
$\epsilon_{iso}(\partial u/\partial x)$	0.2886	11.99	−1635	43470	136
$\epsilon_{iso}(\partial u/\partial y)$	0.2335	49.52	3878	151200	165
ϵ_{axi}	0.3549	11.99	−1635	43470	201
$\epsilon_{\parallel}$	0.07655	11.80	−991.3	34350	151
$\epsilon_{\perp}$	0.1374	11.58	3012	459.0	215

TABLE 6. Curve fits for dissipation (from data of George & Hussein 1991)
$p(\eta) = [C_0 + C_2\eta^2 + C_4\eta^4 + C_6\eta^6]\mathrm{e}^{-A\eta^2}$

where the y-direction is any axis perpendicular to x. These differ considerably from both each other and the locally axisymmetric estimate defined by

$$\epsilon_{axi} = \nu\left\{\frac{5}{3}\overline{\left(\frac{\partial u}{\partial x}\right)^2} + 2\overline{\left(\frac{\partial u}{\partial y}\right)^2} + 2\overline{\left(\frac{\partial w}{\partial x}\right)^2} + \frac{8}{3}\overline{\left(\frac{\partial w}{\partial y}\right)^2}\right\}, \tag{4.5}$$

where the local axis of symmetry has been chosen as the streamwise direction, x. The locally axisymmetric estimate is believed to best represent the actual dissipation in the jet. In spite of the suggestion by George & Hussein (1991) that these results need to be substantiated by further measurement, they certainly constitute the most extensive measurements of dissipation to date in a jet, and the only ones which attempt to deal with its apparent anisotropy. Therefore, the locally axisymmetric estimate will be used below to determine the kinetic energy and component balances, and the pressure–velocity and pressure–strain rate correlations. For the latter purpose, the component dissipations, $\epsilon_{\parallel}$ and $\epsilon_{\perp}$, from the locally axisymmetric estimate will be used where $\epsilon = 2\epsilon_{\perp} + \epsilon_{\parallel}$. Note that curve fits for $\epsilon_{\parallel}$ and $\epsilon_{\perp}$ are included in table 6, and are shown in figure 21(*b*).

Figure 22 shows a plot of the kinetic energy balance in similarity variables. Only the net contribution to the mean convection and turbulent diffusion terms have been plotted. The pressure–diffusion has been obtained as the closing balance, and the viscous diffusion term is negligible because of the high-turbulence Reynolds number. It is apparent from the figure that away from the core region the balance is primarily between production and dissipation, a characteristic of homogeneous and plane shear flows (see Tennekes & Lumley 1972). Near the axis though, the production is small and the remaining terms balance the dissipation.

4.2. *The pressure–velocity correlation*

The difference between the transport dissipation and the directly measured dissipation can be inferred to be primarily the contribution of the missing pressure–velocity moment. If it is assumed that the streamwise gradient of $\overline{pu}/\rho$ can be ignored relative to the radial gradient of $\overline{pv}/\rho$, the latter can be estimated by integrating $\epsilon_{axi} - \epsilon_{tr}$; i.e.

$$\frac{1}{\rho}\overline{pv} \simeq \frac{1}{r}\int_0^r (\epsilon_{tr} - \epsilon_{hom})\, r'\, \mathrm{d}r'. \tag{4.6}$$

Figure 23 shows the profiles of $2\overline{pv}/\rho$ calculated using the dissipation curves from figure 21(*a*). Also show for comparison is the profile of $-\overline{q^2 v}$. The difference between the locally isotropic and locally axisymmetric estimates is striking, with only the latter having the required decrease toward zero at large radius. Also, at least away from the core region, the profile based on the locally axisymmetric dissipation estimate has the same shape as $\overline{q^2 v}$, as suggested by Lumley (1978), and the coefficient is even close to

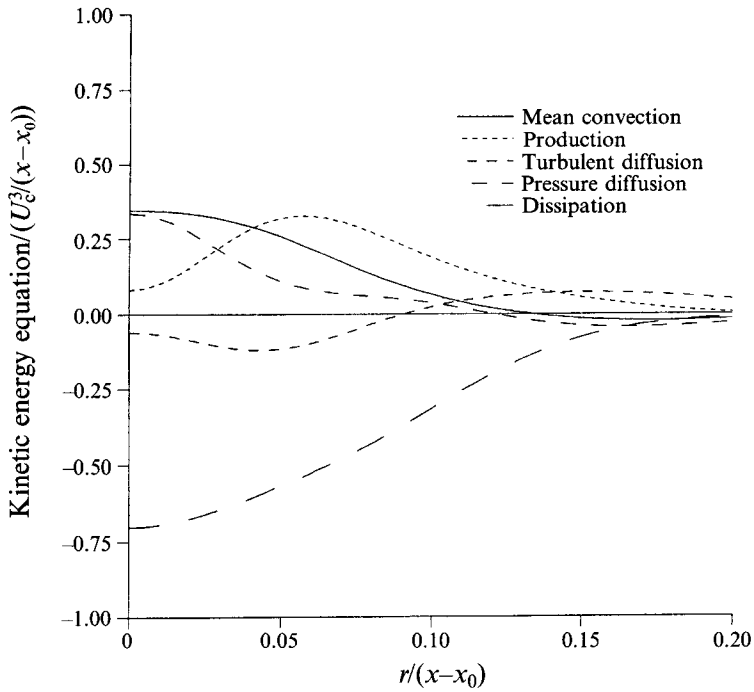

FIGURE 22. Kinetic energy balance.

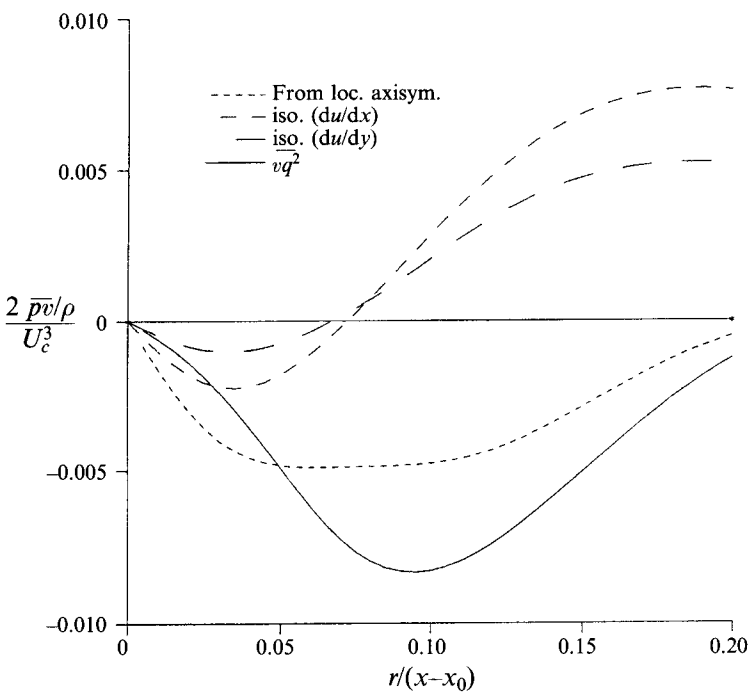

FIGURE 23. Pressure velocity correlation $\overline{pv}/\rho$.

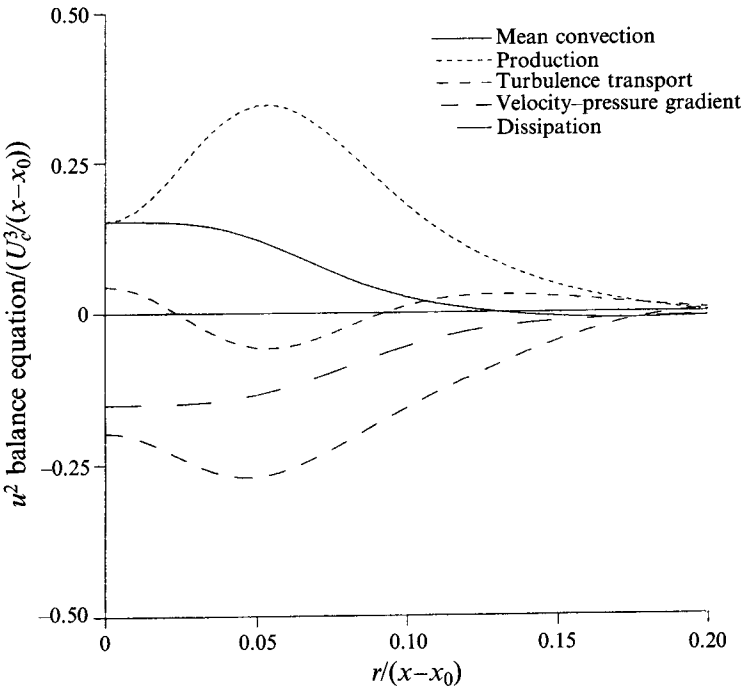

FIGURE 24. Balance of $\overline{u^2}$.

his suggested value of $\frac{2}{5}$. While these results can hardly be regarded as definitive in view of the uncertainty in the dissipation measurements, they would seem to give increased confidence in the locally axisymmetric dissipation estimate. The differences near the core region may be a consequence of a dissipation estimate which is too high, or the non-negligibility of the $\overline{pu}$ contribution there. Alternatively, they may represent mean gradient contributions to pressure–velocity correlation terms previously ignored, but which have been included in the pressure–strain rate models (Lumley 1978), and in calculations of the pressure itself (George, Beuther & Arndt 1984).

4.3. *The component energy and Reynolds stress balances*

The component kinetic energy and Reynolds stress equations for the jet are given by

$\overline{u^2}$ *balance*

$$0 = -\left[U\frac{\partial\overline{u^2}}{\partial x}+V\frac{\partial\overline{u^2}}{\partial r}\right]-\left[\frac{1}{r}\frac{\partial}{\partial r}r\overline{vu^2}+\frac{\partial\overline{u^3}}{\partial x}\right]-\left[2\frac{\overline{u}}{\rho}\frac{\overline{\partial p}}{\partial x}\right]-\left[2\,\overline{uv}\frac{\partial U}{\partial r}+2\overline{u^2}\frac{\partial U}{\partial x}\right]-2\epsilon_{xx}, \quad (4.7)$$

$\overline{v^2}$ *balance*

$$0 = -\left[U\frac{\partial\overline{v^2}}{\partial x}+V\frac{\partial\overline{v^2}}{\partial r}\right]-\left[\frac{1}{r}\frac{\partial}{\partial r}r\overline{v^3}-2\frac{\overline{vw^2}}{r}+\frac{\partial\overline{uv^2}}{\partial x}\right]-\left[2\frac{\overline{v}}{\rho}\frac{\overline{\partial p}}{\partial r}\right]-\left[2\overline{v^2}\frac{\partial V}{\partial r}-2\overline{uv}\frac{\partial V}{\partial x}\right]-2\epsilon_{rr}, \quad (4.8)$$

$\overline{w^2}$ *balance*

$$0 = -\left[U\frac{\partial\overline{w^2}}{\partial x}+V\frac{\partial\overline{w^2}}{\partial r}\right]-\left[\frac{1}{r}\frac{\partial}{\partial r}r\overline{vw^2}+2\frac{\overline{vw^2}}{r}+\frac{\partial\overline{uw^2}}{\partial x}\right]-2\left[\frac{\overline{w}}{\rho r}\frac{\overline{\partial p}}{\partial\theta}\right]-2\frac{V}{r}\overline{w^2}-2\epsilon_{\theta\theta}, \quad (4.9)$$

$\overline{uv}$ balance

$$0 = -\left[U\frac{\partial}{\partial x}\overline{uv} + V\frac{\partial}{\partial r}\overline{uv}\right] - \left[\frac{1}{r}\frac{\partial}{\partial r}r\overline{uv^2} - \frac{\overline{uw^2}}{r} + \frac{\partial\overline{vu^2}}{\partial x}\right]$$
$$-\left[\frac{\overline{u}\,\overline{\partial p}}{\rho\,\partial r} + \frac{\overline{v}\,\overline{\partial p}}{\rho\,\partial x}\right] - \left[\overline{uv}\frac{\partial V}{\partial r} + \overline{v^2}\frac{\partial U}{\partial r} + \overline{u^2}\frac{\partial V}{\partial x} + \overline{uv}\frac{\partial U}{\partial x}\right] - 2\epsilon_{xr}. \quad (4.10)$$

These can be identified as the mean convection, turbulence transport, work done by pressure gradient, turbulence production, and component dissipation respectively. (Note that the customary decomposition of the pressure–work term into pressure diffusion and pressure–strain rate has been deferred to the next section since only the pressure–work can be obtained without assumptions). The viscous diffusion terms are not included since they are negligible for this flow. For locally axisymmetric turbulence with the preferred axis in the x-direction, $\epsilon_{xx} = \epsilon_{\parallel}$ and $\epsilon_{rr} = \epsilon_{\theta\theta} = \epsilon_{\perp}$, while $\epsilon_{xr} = 0$.

Figures 24–27 show the balances for (4.7)–(4.10). The pressure–work term has been obtained as the closing balance. Particularly interesting is the role of this term which is to remove energy from the $\overline{u^2}$ component equation (where energy is primarily produced from the mean flow), and to redistribute it to the other two components. This is most striking for the $\overline{w^2}$ component equation where there is negligible production and the balance is almost entirely between the energy transferred by the pressure gradient term, and the dissipation.

4.4. *The pressure–strain rate terms*

It is customary (see Tennekes & Lumley 1972) to separate the pressure-gradient terms into pressure–diffusion and pressure–strain rate terms. For the axisymmetric jet the appropriate decompositions are

$$\frac{1}{\rho}\overline{u\frac{\partial p}{\partial x}} = \frac{1}{\rho}\frac{\partial}{\partial x}\overline{pu} - \frac{1}{\rho}\overline{p\frac{\partial u}{\partial x}}, \quad (4.11)$$

$$\frac{1}{\rho}\overline{v\frac{\partial p}{\partial r}} = \frac{1}{\rho}\frac{\partial}{\partial r}\overline{pv} - \frac{1}{\rho}\overline{p\frac{\partial v}{\partial r}}, \quad (4.12)$$

$$\overline{\frac{w}{\rho r}\frac{\partial p}{\partial\theta}} = \left[\frac{1}{\rho r}\frac{\partial}{\partial\theta}\overline{pw} + \frac{\overline{pv}}{r}\right] - \frac{1}{\rho r}\overline{p\left(\frac{\partial w}{\partial\theta} + v\right)}, \quad (4.13)$$

$$\frac{1}{\rho}\left(\overline{u\frac{\partial p}{\partial r}} + \overline{v\frac{\partial p}{\partial x}}\right) = \frac{1}{\rho}\left[\frac{\partial}{\partial r}\overline{pu} + \frac{\partial}{\partial x}\overline{pv}\right] - \overline{p\left(\frac{\partial u}{\partial r} + \frac{\partial v}{\partial x}\right)}. \quad (4.14)$$

The last term on the right-hand side in each equation is the pressure–strain rate term, while the remainder represent the pressure–diffusion. Note that the sum of equations (4.11)–(4.13) yields the pressure–diffusion term of the kinetic energy equation since the pressure–strain rate terms add to zero by continuity.

Figure 28 shows the four pressure–strain rate terms calculated from (4.11)–(4.14), and makes clear their role in redistributing the turbulence kinetic energy. These have been obtained by assuming that

$$\frac{1}{\rho}\frac{\partial}{\partial x}\overline{pu} \ll \frac{1}{\rho}\overline{p\frac{\partial u}{\partial x}},$$

in equation (4.11), and that

$$\frac{1}{\rho}\left[\frac{\partial}{\partial r}\overline{pu} + \frac{\partial}{\partial x}\overline{pv}\right] \ll \overline{\frac{p}{\rho}\left(\frac{\partial u}{\partial r} + \frac{\partial v}{\partial x}\right)},$$

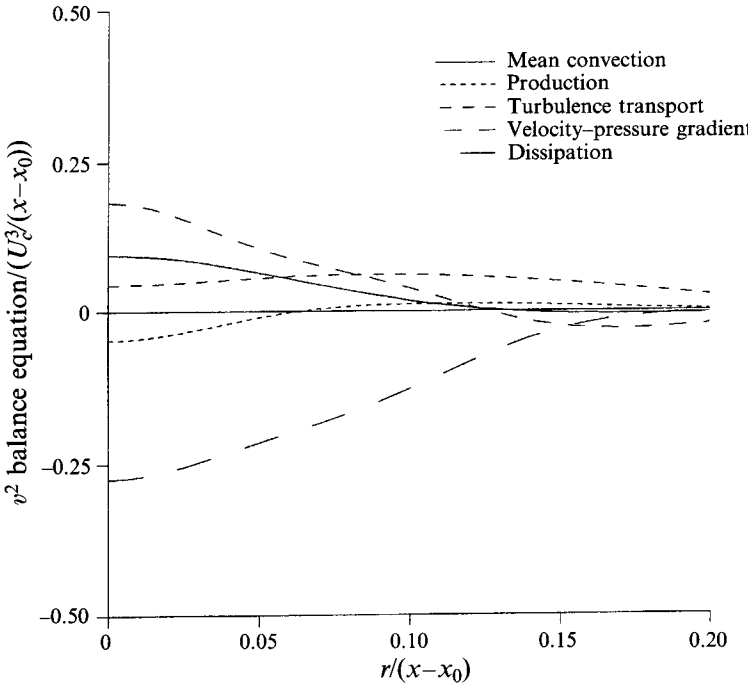

FIGURE 25. Balance of $\overline{v^2}$.

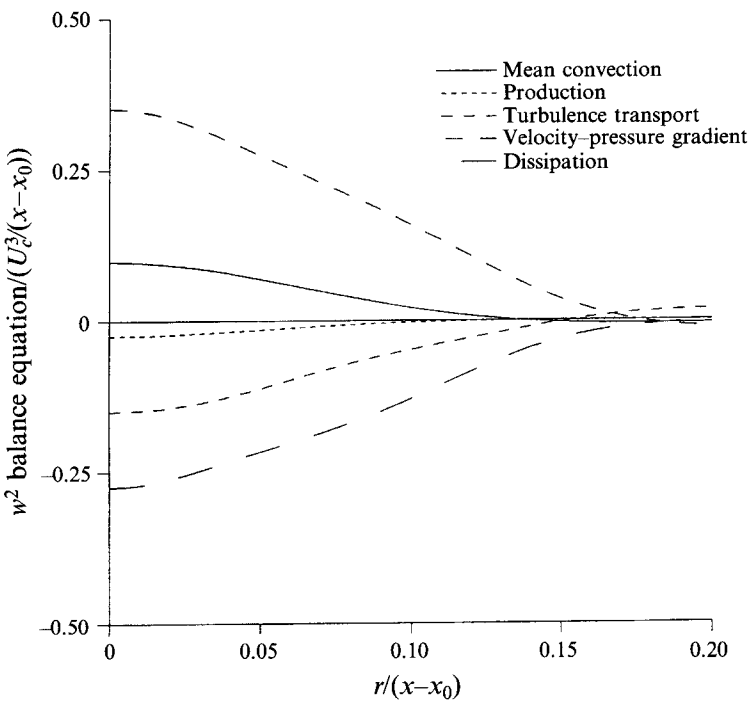

FIGURE 26. Balance of $\overline{w^2}$.

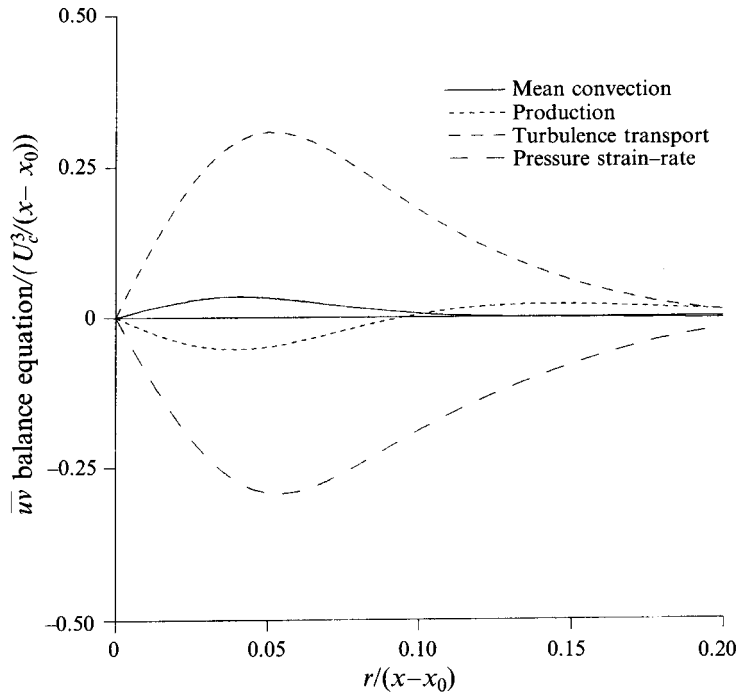

FIGURE 27. Balance of $\overline{uv^2}$.

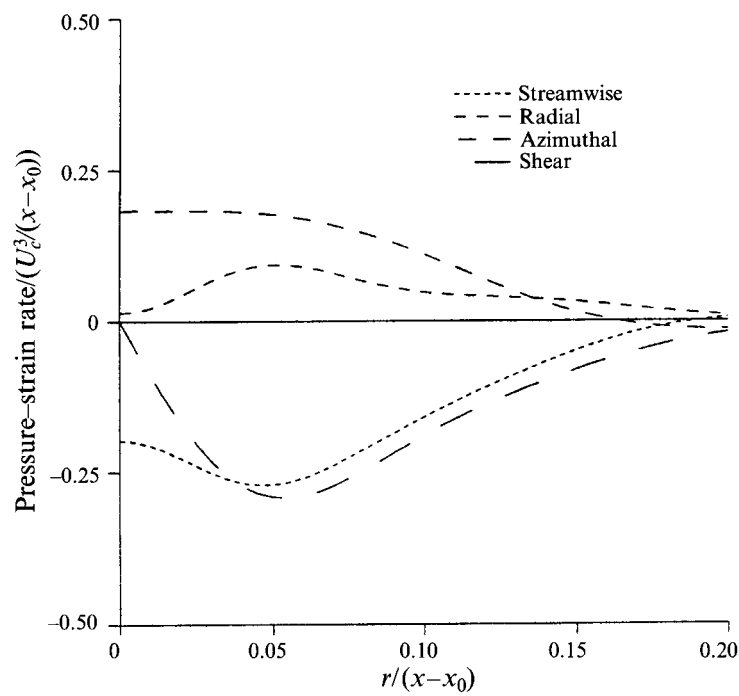

FIGURE 28. Pressure–strain rate correlations.

in equation (4.14). The terms involving $\overline{pv}$ utilized the results of §4.2. Note that $\partial\overline{pw}/\partial\theta = 0$ because of the axial symmetry of the jet.

5. Summary and conclusions

Measurements of the turbulent velocity field of an axisymmetric jet using burst-mode laser Doppler anemometer (LDA) and stationary and flying hot-wire (SHW and FHW respectively) techniques have been reported for all moments up to the third order. The LDA and FHW results differ substantially from the SHW results, especially away from the centre of the jet where the local turbulence intensity is a minimum. The observed differences are consistent with the well-known hot-wire errors in high-intensity turbulent flows, in particular, cross-flow, rectification and drop-out.

Particular care was taken to check whether or not the equations of motion for a free axisymmetric jet were satisfied. The LDA and FHW results were shown to satisfy both the second-order differential and integral forms of the momentum equation for a free jet to within the experimental accuracy of the measurements and integration. The SHW results of this investigation, on the other hand showed substantial deviations which were consistent with the hot-wire errors. A similar analysis of the SHW results of other investigators showed deviations which suggest that the flows being measured were strongly influenced by the presence of the return flow in the facility as well as by experimental errors arising from the high turbulence intensity.

Subsequent to the work reported herein, but already published (George & Hussein 1991), flying hot-wire experiments were conducted in the same jet for the purpose of directly measuring the dissipation. Those measurements showed the dissipation to be locally axisymmetric. The dissipation estimates, from the flying wire experiments were utilized here to obtain a satisfactory turbulence energy balance and to provide some insight into the missing pressure–velocity and pressure–strain rate correlations. The estimates of the pressure–velocity correlation based on a locally isotropic dissipation were physically unrealistic, but the locally axisymmetric dissipation gave reasonable behaviour at large radius, thus lending additional support to the local axisymmetry hypothesis. The energy and Reynolds stress balances clearly show that the balances in the core region were dominated by the mean convection and secondary terms. This is in contrast to the flow away from the core in which, like homogeneous shear flows, the primary balance was among the production, pressure–strain rate, and dissipation terms.

Almost concurrent with the experiments described here has been a somewhat parallel effort by Panchapakesan & Lumley (Panchapakesan 1990; Panchapakesan & Lumley 1993) at Cornell University. Their jet results are in good agreement with those reported here, but with several slight but important differences. In particular, the off-axis peaks in the normalized Reynolds stress and cross-moments were slightly lower (5–10 %) and there were substantial differences (30–50 %) at large radius ($\eta > 0.12$) in many of the moments. The former can be understood using the analysis of Appendix C where it is argued that the cross-moments should scale with $U_c^3\,\mathrm{d}\delta/\mathrm{d}x$ instead of U_c^3. Also $\mathrm{d}\delta/\mathrm{d}x$ should decrease toward an infinite Reynolds number limit as the source Reynolds number increases. The source Reynolds number in the Panchapakesan/Lumley experiment was an order of magnitude lower than in the experiments reported here (1.1×10^4 *vs.* 10^5), and the observed spreading rate was slightly larger (0.96 *vs.* 0.94). Thus both of these results may well be correct, the difference resulting from the different Reynolds numbers of the experiment. The effect on the measured moments, however, would be opposite to that observed, therefore an explanation must be sought

elsewhere. The discrepancies can probably be attributed to the relatively high effective turbulence intensity in the Panchapakesan/Lumley experiment than here (about 20%). This is because their probe velocity was approximately equal to the velocity of the mean flow at the centreline (at $x/D = 60$), whereas here it was about twice. From the expansions of table 2, it is clear that the higher moments will be most sensitive to the effective turbulence intensity and especially at large radius. Therefore the profiles presented here perhaps have the better claim, especially since the LDA and FHW agree. On the other hand, the differences may simply reflect the different boundary and initial conditions.

In conclusion, the results of the present experiment (and those of Panchapakesan & Lumley as well) make it clear that previous axisymmetric jet studies leave much to be desired, and probably should not be trusted – both because of the techniques employed and the facilities utilized. There remain, however, some important questions to be explored; including the full implications of the similarity analysis of Appendix C, the exact nature of the dissipation and its relation to local axisymmetry and similarity theory, and the Reynolds-number dependence of this flow.

This work was initiated in the early 1980s at the Turbulence Research Laboratory, and formed a portion of the PhD dissertations of H.J.H. and S.P.C. It has benefited from the contributions of a number of researchers who have not been listed as co-authors. Of particular importance have been the contributions of C. B. Baker (now deceased), D. X. Peng, A. A. Seif, R. Suhoke, Jr, J. Tan-atichat, S. H. Woodward, and especially D. B. Taulbee. The authors are grateful to these, and to E. Graber for typing numerous revisions of the manuscript.

This work was initiated under the auspices of the Air Force Office of Scientific Research (grant no. F4962080C0053) through a three university cooperative program at the University at Buffalo, SUNY, the Illinois Institute of Technology, and the University of Minnesota. The primary sponsor of the measurements reported here was the National Science Foundation, Fluid Mechanics Program under grant no. MSM8316833.

Appendix A. Justification of equation (3.8) for the momentum integral

The full averaged momentum equation for the axisymmetric jet can be written with the help of the continuity equation as

$$\frac{\partial(U^2+\overline{u^2})}{\partial x}+\frac{1}{r}\frac{\partial}{\partial r}r(UV+\overline{uv}) = -\frac{1}{\rho}\frac{\partial P}{\partial x}+\nu\nabla^2 U, \tag{A 1}$$

$$\frac{\partial(UV+\overline{uv})}{\partial x}+\frac{1}{r}\frac{\partial}{\partial r}r(V^2+\overline{v^2}) = -\frac{1}{\rho}\frac{\partial P}{\partial r}+\nu\nabla^2 V+\frac{\overline{w^2}}{r}. \tag{A 2}$$

By integrating (A 2) with respect to r from r to infinity, and substituting its x-derivative into (A 1), it follows that

$$\begin{aligned}\frac{\partial}{\partial x}(U^2+u^2)+\frac{1}{r}\frac{\partial}{\partial r}r(UV+\overline{uv}) = &-\int_r^\infty \frac{\partial^2}{\partial x^2}(UV+\overline{uv})\,dr'+\frac{\partial}{\partial x}(V^2+\overline{v^2})\\ &-\int_r^\infty \frac{\partial}{\partial x}\left(\frac{V^2+\overline{v^2}}{r'}\right)dr'+\int_r^\infty \frac{\partial}{\partial x}\left(\frac{\overline{w^2}}{r'}\right)dr'+\int_r^\infty \frac{\partial}{\partial x}(\nu\nabla^2 V)\,dr'+\nu\nabla^2 U.\end{aligned} \tag{A 3}$$

Note that V and the turbulence quantities have been assumed to go to zero as $r\to\infty$.

Equation (A 3) can be integrated across the entire jet to yield

$$\frac{\mathrm{d}}{\mathrm{d}x}\int_0^\infty [U^2+\overline{u^2}-\tfrac{1}{2}(\overline{v^2}+\overline{w^2})]\,r\,\mathrm{d}r = -\frac{1}{2}\frac{\mathrm{d}^2}{\mathrm{d}x^2}\int_0^\infty (UV+\overline{uv})\,r^2\,\mathrm{d}r+\frac{1}{2}\frac{\mathrm{d}}{\mathrm{d}x}\int_0^\infty V^2\,r\,\mathrm{d}r$$
$$+\frac{\mathrm{d}}{\mathrm{d}x}\left[\frac{1}{2}\int_0^\infty (\nu\nabla^2 V)\,r^2\,\mathrm{d}r\right]+\int_0^\infty (\nu\nabla^2 U)\,r\,\mathrm{d}r. \quad \text{(A 4)}$$

This can be integrated with respect to x from the source to location x to yielding

$$\int_0^\infty [U^2+\overline{u^2}-\tfrac{1}{2}(\overline{v^2}+\overline{w^2})]\,r\,\mathrm{d}r-\frac{M_0}{2\pi}$$
$$= \underbrace{-\frac{1}{2}\frac{\mathrm{d}}{\mathrm{d}x}\int_0^\infty [UV+\overline{uv}]\,r^2\,\mathrm{d}r\Big|_0^x}_{(a)}+\underbrace{\frac{1}{2}\int_0^\infty V^2\,r\,\mathrm{d}r}_{(b)}$$
$$+\underbrace{\frac{1}{2}\int_0^\infty (\nu\nabla^2 V)\,r^2\,\mathrm{d}r\Big|_0^x}_{(c)}+\underbrace{\int_0^x\left[\int_0^\infty \nu\nabla^2 U\,r\,\mathrm{d}r\right]\mathrm{d}x'}_{(d)} \quad \text{(A 5)}$$

If the terms on the right-hand side of (A 5) can be shown to be negligible compared to $M_0/2\pi$, then (3.8) follows immediately. Each of the integrals on the right-hand side can be computed using the appropriate similarity forms and the empirical curve fits of table 4. The first integral is the largest, but is less than $0.02M_0$; the remainder are several orders of magnitude less. This approach, however, ignores a possible significant contribution from the last two terms near $x = 0$. Therefore the following order of magnitude analysis is useful.

From the left-hand side of (A 5) (or equation (3.1)) it follows that

$$M_0 \sim U_0^2 D^2 \sim U_s^2 \delta^2.$$

Term (a)

At location x, both UV and $\overline{uv}$ can be shown to be of order $U_s^2\,\delta/L$ (the former from continuity, the latter from the necessity of retaining the Reynolds stress in the x-momentum equation) it follows that

$$\frac{1}{M}[a] \sim \frac{1}{M_0}\frac{1}{L}U_s^2\frac{\delta}{L}\delta^3 \sim \left(\frac{\delta}{L}\right).$$

This is consistent with the boundary-layer approximation and the value of 0.02 obtained by substitution of the measured profiles. At the exit plane ($x = 0$), if L_0 is a lengthscale characteristic of the streamwise development of the local shear layer and δ_0 is its thickness, then $V \sim U_0\,\delta_0/L_0$ so that the mean velocity term then can be estimated as

$$\frac{1}{M}[a(0)] \sim \frac{1}{M_0}\frac{1}{L_0}U_0\,U_0\frac{\delta_0}{L_0}D^2\delta_0 \sim \left(\frac{\delta_0}{L_0}\right)^2.$$

Since the shear layer at the lip also develops slowly $\delta_0/L_0 \ll 1$ and this term is also negligible. The turbulence contribution is identically zero if the boundary layer at the lip is laminar. If not, $-\overline{uv} \sim u_*^2$, the friction velocity, which can be estimated from the boundary-layer equation as $U_0\,\delta_0/L_0$ thus yielding the same order of magnitude as for the mean term.

Term (b)

Since $V \sim U_s \delta/L$ it follows that

$$\frac{1}{M_0}[b] \sim \frac{1}{M_0} U_s^2 \left(\frac{\delta}{L}\right)^2 \delta^2 \sim \left(\frac{\delta}{L}\right)^2.$$

Thus this term is an order of magnitude smaller than term (*a*), a fact confirmed by integration of the measured profiles.

Term (c)

There are two contributions to this term, one at the downstream location x, the other at the exit plane. At location x, which is presumed to be in the self-preserving region, the radial gradients of V scale with δ so that

$$\frac{1}{M_0}[c(x)] \sim \left(\frac{1}{U_s^2 \delta^2}\right) \nu U_s \frac{\delta}{L} \frac{1}{\delta^2} \delta^3 \sim \frac{\nu}{U_s L},$$

which is typically $10^{-3} - 10^{-4}$.

At the exit plane, if the jet is presumed to exit from a nozzle into free space the primary contribution is from the very thin boundary layer coming off of the jet lip. Estimating this layer thickness by the boundary-layer thickness at the exit, δ_0, yields

$$\frac{1}{M_0}[c(0)] \sim \frac{1}{U_0^2 D^2} \nu U_0 \frac{\delta_0}{L_0} \frac{1}{\delta_0^2} D^2 \delta_0 \sim \frac{\nu}{U_0 \delta_0} \left(\frac{\delta_0}{L_0}\right),$$

where L_0 is a scale characteristic of the streamwise gradient of U in the developing shear layer at the exit. Since δ_0/L_0 can be no larger than order one, for $U_0 = 55$ m/s, $\delta_0 \sim 1$ mm in air, this term is less than 10^{-3}–10^{-4}.

Term (d)

An upper bound for the contribution of this term can be estimated by using the value of the integrand at the origin. Using the same arguments as above,

$$\frac{1}{M_0}[d(0)] \sim \frac{1}{U_0^2 D^2} \nu U_0 \frac{1}{\delta_0^2} D \delta_0 L \sim \frac{\nu}{U_0 L} \left(\frac{D}{\delta_0}\right).$$

Using the values above with $D \sim 0.025\ m$ and $L \sim 100D$ gives a value of less than 10^{-3}.

It should be noted, however, that both terms (*c*) and (*d*) could be significantly increased by the presence of a wall through which the jet exits. This has been previously noted by Schneider (1985) using matched asymptotic expansions.

Appendix B. A model for the effect of confinement on momentum conservation

It has been argued in §3.2 that the failure of earlier experiments to satisfy the momentum integral can be attributed to the effects of confinement on the jet. In particular, it was suggested that the presence of walls at a finite radius causes the entrainment to be fed by a reverse flow outside the jet (see figure 29). Since the contribution of this return flow to the momentum integral is positive (negative momentum going backwards), it is the sum of this momentum and that in the jet which is equal to M_0. Thus the return flow 'steals momentum from the jet', and thereby

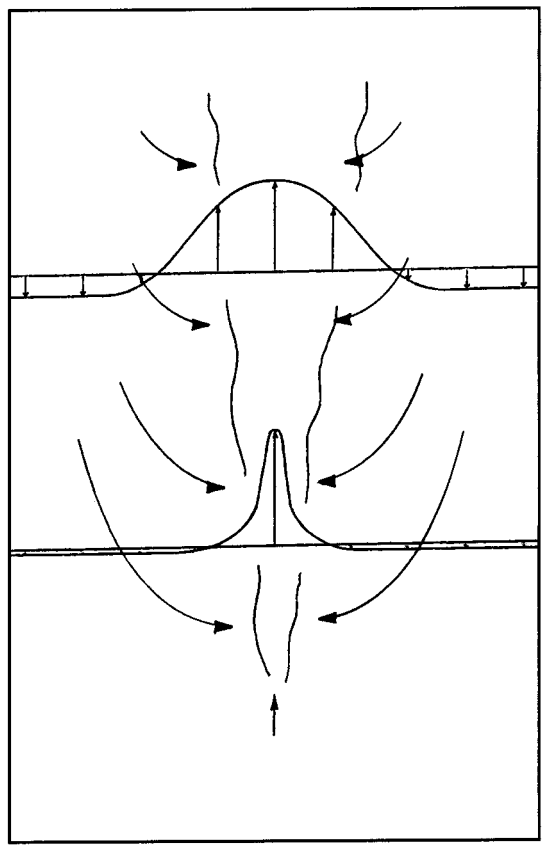

FIGURE 29. Schematic showing return flow in a confined jet.

progressively modifies it from the jet which would be observed in an infinite environment. The purpose of this Appendix is to provide a model for this phenomenon, and an estimate as to how it relates to the jet and room parameters.

To first order, the momentum integral at each cross-section of the room must be equal to the rate at which momentum is added at the source. Note that this ignores the second-order contributions due to turbulence and mean pressure variations, as well as viscous effects on the walls. Considering the flow to consist of two parts, a jet-like part and a return flow, yields the following momentum constraint:

$$\iint_{jet} U^2 \,\mathrm{d}A + \iint_{return} U^2 \,\mathrm{d}A = M_0. \tag{B 1}$$

Since mass must also be conserved the return flow must balance the jet flow so that

$$\iint_{jet} U \,\mathrm{d}A = \iint_{return} U \,\mathrm{d}A. \tag{B 2}$$

If the return flow can be approximated as uniform across the cross-section, then (B 2) reduces to

$$\iint_{jet} U \,\mathrm{d}A = U_R A_R, \tag{B 3}$$

where U_R is the return flow velocity at a given x-location and A_R is the cross-sectional area of the room there. (Note that the area taken up by the jet-like part of the flow is ignored to this approximation.) Similarly, (B 1) can be approximated by

$$\iint_{jet} U^2 \,\mathrm{d}A + U_R^2 A_R = M_0. \tag{B 4}$$

The velocity profile in the jet-like part of the flow can be written in similarity-like variables using the local jet momentum integral as

$$U = BM^{\frac{1}{2}}x^{-1}f(r/x), \tag{B 5}$$

where

$$M(x) \equiv \int_{jet} U^2 \,\mathrm{d}A. \tag{B 6}$$

A convenient choice for the profile $f(r/x)$ is the Gaussian one so that

$$f(\eta) = \exp[-C\eta^2], \tag{B 7}$$

where as before $\eta = r/x$.

Note that (B 6) can be satisfied by this profile only if

$$\frac{2\pi B^2}{4C} = 1. \tag{B 8}$$

Substitution of equations (B 5) and (B 7) into (B 3) yields the x-dependent return flow velocity as

$$U_R = \frac{\pi B}{CA_R} M^{\frac{1}{2}}x = \frac{2}{B} M^{\frac{1}{2}}x. \tag{B 9}$$

Further substitution into equation (B 4) and use of equation (B 7) yields the momentum constraint as

$$\frac{M}{M_0} = \left[1 + \frac{16}{\pi B^2}\left(\frac{x}{D}\right)^2 \frac{A_0}{A_R}\right]^{-1}, \tag{B 10}$$

where D is the jet exit diameter ($A_0 = \frac{1}{4}\pi D^2$). Thus to first order, the local momentum in the jet-like part of the flow is diminished as x/D increases.

Equation (B 10) can be used to estimate the room size required to return a given level of momentum in the jet. For the experiment described here $A_0 = 4.9 \times 10^{-4}\ \mathrm{m}^2$ and $A_R = 23.9\ \mathrm{m}^2$ so that $A_R A_0 = 4.9 \times 10^{-4}$. From §3.1, $B \simeq 6.5$ is an appropriate choice, so that the momentum ratio at $x/D = 70$ is given by $M/M_0 = 0.99$. Thus the experiment reported here should closely resemble a jet in an infinite environment, at least by this criterion.

Appendix C. Similarity analysis of the axisymmetric turbulent jet

The traditional similarity analysis of jet assumes *a priori* that all jets will be asymptotically alike and characterized by the hypothetical point source jet (see Monin & Yaglom 1971; Townsend 1976). These ideas were recently challenged by George (1989) who argued that real jets, in fact, retained forever a dependence on the conditions at the source. This Appendix briefly summarizes those arguments and emphasizes points of particular interest here.

Solutions are sought to the averaged momentum equation for which the velocity and Reynolds stress are represented by

$$U = U_s(x)f(\eta), \tag{C 1}$$

$$-\overline{uv} = R_s(x)g(\eta), \tag{C 2}$$

where $$\eta = r/\delta(x). \tag{C 3}$$

It is important to note that it is never assumed that $R_s = U_s^2$, nor will it be found to be so.

The x-momentum equation to first order is given by

$$U\frac{\partial U}{\partial x} + V\frac{\partial U}{\partial y} = -\frac{1}{r}\frac{\partial}{\partial r} r\overline{uv}. \tag{C 4}$$

Substitution of (C 1)–(C 3) yields

$$-f^2 - \frac{f'}{\eta}\int_0^\eta f(\bar{\eta})\,\bar{\eta}\,\mathrm{d}\bar{\eta} = \left[\frac{R_s}{U_s^2\,\mathrm{d}\delta/\mathrm{d}x}\right]\frac{(\eta g_{12})'}{\eta}, \tag{C 5}$$

where (3.8), the integral momentum equation, has been used to deduce that $U_s \sim x^{-1}$. It is clear that a similarity solution can exist only if the bracketed term is constant, i.e.

$$R_s \propto U_s^2\,\mathrm{d}\delta/\mathrm{d}x. \tag{C 6}$$

Note that the constant of proportionality may depend on the source conditions, and that similarity of the velocity and Reynolds stress profiles requires neither a linear growth rate nor power law solutions.

It is easy to see from (C 5) why the previous analysis with $R_s = U_s^2$ have been accepted. If the constant of proportionality from (C 6) is absorbed into the Reynolds stress function $g_{12}(\eta)$, then (C 5) will be the same for all jets, independent of source conditions or growth rate, $\mathrm{d}\delta/\mathrm{d}x$. Thus, if U/U_c is plotted as a function of $y/\delta_{\frac{1}{2}}$, then all (properly measured) experiments should produce the same profile, regardless of $\mathrm{d}\delta/\mathrm{d}x$ and source conditions. Because $\mathrm{d}\delta/\mathrm{d}x$ itself depends on the source conditions it would be wrong to assume from this that all jets are asymptotically similar. In fact, the Reynolds stress which when plotted as $\overline{uv}/U_c^2$ will vary from experiment to experiment (or in some non-jet flows, from station to station, cf. George 1989) because its own scale represented in these variables is $U_c^2\,\mathrm{d}\delta_{\frac{1}{2}}/\mathrm{d}x$.

The x-dependence of δ can be examined by considering (4.1) for the kinetic energy. The kinetic energy, radial transport, and dissipation can be represented by

$$\tfrac{1}{2}\overline{q^2} = K_s(x)\,k(\eta), \tag{C 7}$$

$$-\overline{pv} + \tfrac{1}{2}\overline{q^2 v} = T_s(x)\,t(\eta), \tag{C 8}$$

$$\epsilon = D_s(x)\,e(\eta). \tag{C 9}$$

Substitution of these into (4.1) (with the neglect of the streamwise transport terms) yields

$$\left[\frac{\delta}{K_s}\frac{\mathrm{d}K_s}{\mathrm{d}x}\right]fk - \left[\frac{\mathrm{d}\delta}{\mathrm{d}x}\right]\frac{k'}{\eta}\int_0^\eta f(\bar{\eta})\,\bar{\eta}\,\mathrm{d}\bar{\eta} = \left[\frac{T_s}{K_s U_s}\right]\frac{(\eta t)'}{\eta} + \left[\frac{R_s}{K_s}\right]g_{12}f' - \left[\frac{D_s\delta}{K_s U_s}\right]e. \tag{C 10}$$

It follows immediately that the similarity solutions can exist only if all of the bracketed terms have the same x-dependence, i.e.

$$\frac{\delta}{K_s}\frac{\mathrm{d}K_s}{\mathrm{d}x} \sim \frac{T_s}{K_s U_s} \sim \frac{R_s}{K_s} \sim \frac{D_s\delta}{K_s U_s} \sim \frac{\mathrm{d}\delta}{\mathrm{d}x}. \tag{C 11}$$

It is straightforward to show that $K_s \sim U_s^2$, so that $T_s \sim U_s^3\,\mathrm{d}\delta/\mathrm{d}x$ and $D_s \sim (U_s^3/\delta)\,\mathrm{d}\delta/\mathrm{d}x$. Thus all of the cross-moments of second and third order do not scale with the velocity alone, but rather its product (to the appropriate power) with the growth rate. Therefore, as with Reynolds stress, the moments normalized with U_c alone should be expected to vary from experiment to experiment.

The dissipation result of (C 11) can be used to show that the axisymmetric jet does indeed grow linearly, for all source conditions (unlike the plane jet, for example). At infinite Reynolds number the rate of dissipation is entirely governed by the rate of spectral energy transfer to the viscous scales so that $\epsilon \sim q^3/l$ where l is the physical length scale associated with the energy-containing eddies. For this flow $l \sim \delta$ so that $D_s \sim U_s^3/\delta$, with the result that $\mathrm{d}\delta/\mathrm{d}x = \text{constant}$. Thus the infinite Reynolds number jet grows linearly, albeit at a rate still dependent on the source conditions (e.g. exit velocity profile).

For very low Reynolds number (but still fully turbulent), the dissipation and energy-containing ranges overlap so that $\epsilon \sim \nu q^2/l^2$ (see Tennekes & Lumley 1972). It follows that $D_s \sim \nu U_s^2/\delta^2$ and that $\mathrm{d}\delta/\mathrm{d}x \sim \nu/U_s\delta$. Thus since $U_s\delta = \text{const}$ (from the momentum integral), the low-Reynolds-number jet also grows linearly, albeit at a rate inversely proportional to Reynolds number.

While neither the low nor infinite Reynolds number limits is probably a very good description of laboratory jets, it is reasonable to expect a linear growth at a rate which is only asymptotically independent of source Reynolds number. Thus all measurements of growth rate and cross-moments will reflect the source Reynolds number at which the experiment is carried out. Most importantly, since the jet evolves at constant Reynolds number regardless of how it is generated (because of the momentum constraint), the collapse among experiments will not be improved by increasing distance downstream (at least for this flow).

REFERENCES

BAKER, C. B. 1980 An analysis of the turbulent buoyant jet. PhD dissertation, Pennsylvania State University, University Park, PA.

BAKER, C. B., GEORGE, W. K. & TAULBEE, D. B. 1980 An analysis of the axisymmetric turbulent buoyant jet. *Proc. 7th Intl Heat Trans. Conf. Sept. 6–10.* Munich, Germany

BATURIN, V. 1972 *Fundamentals of Industrial Ventilation.* Pergamon.

BEUTHER, P. D., SHABBIR, A. & GEORGE, W. K. 1987 X-wire response in turbulent flows with high intensity turbulence and low mean velocity. *Proc. ASME Symp. on Thermal Anemometry* (ed. D. Stock), FED V53, pp. 39–42. Cincinnati, OH.

BUCHHAVE, P. 1976 Biasing errors in individual particle measurements with the LDA-counter signal processors. In *Proc. LDA Symp. Copenhagen*, 1975, pp. 258–278. Dantec, Copenhagen.

BUCHHAVE, P., GEORGE, W. K. & LUMLEY, J. L. 1979 The measurement of turbulence with the laser-Doppler anemometer. *Ann. Rev. Fluid Mech.* **11**, 443–503.

CAPP, S. P. 1983 Experimental investigation of the turbulent axisymmetric jet. PhD dissertation, University at Buffalo, SUNY.

CAPP, S. P. & GEORGE, W. K. 1982 Measurements in an axisymmetric jet using a two-color LDA and burst processing. *Proc. Intl Symp. on Appl. of LDA to Fluid Mechanics* (ed. P. Durao *et al.*), §1.2, Lisbon, Portugal.

CORRSIN, S. 1943 Investigation of flow in an axially symmetrical heated jet of air. NACA, Wash. Wartime Report, W-94.

CORRSIN, S. & KISTLER, A. L. 1955 *National Advisory Committee Aeronaut. Tech. Notes* 3133.

CORRSIN, S. & UBEROI, M. S. 1950 Further experiments of the flow and heat transfer in a heated jet. *NACA Rep.* 998.

CORRSIN, S. & UBEROI, M. S. 1951 Spectra and diffusion in a round turbulent jet. *NACA Rep.* 1940 (originally published as *NACA Tech. Note* 2124, Aug. 1950).

GEORGE, W. K. 1979 Processing of random signals. *Dynamic Measurements in Unsteady Flow, Proc. of the Dynamic Flow Conf. 1978* (ed. P. Buchhave *et al.*), pp. 757–800. Dantek, Copenhagen.

GEORGE, W. K. 1988 Quantitative measurement with the burst-mode laser-Doppler anemometer. *Expl Thermal Fluid Sci.* **1**, 29–40.

GEORGE, W. K. 1989 The self-preservation of turbulent flows and its relation to initial conditions

and coherent structures. *Advances in Turbulence* (ed. W. K. George & R. E. A. Arndt), pp. 39–72. Hemisphere.

GEORGE, W. K. 1990 Governing equations, experiments and the experimentalist. *Expl Thermal Fluid Sci.* **3**, 557–566.

GEORGE, W. K., BEUTHER, P. D. & ARNDT, R. E. A. 1984 Pressure spectra in turbulent free shear flows. *J. Fluid Mech.* **148**, 155–191.

GEORGE, W. K., BEUTHER, P. D. & SHABBIR, A. 1989 Polynomial calibrations for hot wires in thermally varying flows. *Expl Thermal Fluid Sci.* **2**, 230–235.

GEORGE, W. K., CAPP, S. P., SEIF, A. A., BAKER, C. B. & TAULBEE, D. B. 1988 A study of the turbulent axisymmetric jet. *J. Engng Sci. King Saud Univ.* **14**, 85–93.

GEORGE, W. K. & HUSSEIN, H. J. 1991 Locally axisymmetric turbulence. *J. Fluid Mech.* **233**, 1–23.

GEORGE, W. K., SEIF, A. A. & BAKER, C. B. 1982 Momentum balance considerations in axisymmetric turbulent jets. SUNY/Buffalo, *Turbulence Research Laboratory Report TRL* 115.

HINZE, J. O. 1975 *Turbulence.* McGraw-Hill.

HINZE, J. O. & VAN DER HEGGE ZIJNEN, B. G. 1949 Transfer of heat and matter in the turbulent mixing zone of an axially symmetrical jet. *Appl. Sci. Res.* A **1**, 435–461.

HUSSAIN, A. M. K. F. & CLARK, A. R. 1977 Upstream influence in the near field of a plane turbulent jet. *Phys. Fluids* **20**, 1460.

LEHRMANN, B. 1986 Laser Doppler measurements in a turbulent free jet. *DFVLR-Forschungsbericht*, pp. 55–86.

LIST, E. J. 1979 In *Mixing in Inland and Coastal Waters*, Chap. 9 (ed. H. B. Fisher *et al.*). Academic Press.

LIST, E. J. 1980 Mechanics of turbulent buoyant jets and plumes. In *Turbulent Jets and Plumes* (ed. W. Rodi), pp. 1–68. Pergamon.

LUMLEY, J. L. 1978 Computational modelling of turbulent flows. *Adv. Appl. Mech.* **18**, 123–126.

MONIN, A. S. & YAGLOM, A. M. 1971 *Statistical Fluid Mechanics, Mechanics of Turbulence*, vol. 1, MIT Press, Cambridge, MA.

MOREL, T. 1975 Comprehensive design of axisymmetric wind tunnel contractions. *Trans. ASME* I: *J. Fluids Engng* **97**, 225–233.

MORTON, B., TAYLOR, G. I. & TURNER, J. S. 1956 Turbulent gravitational convection from maintained and instantaneous sources. *Proc. R. Soc.* **243**, 1–23.

PANCHAPAKESAN, N. R. 1990 Turbulence measurements in axisymmetric jets of air and helium. PhD dissertation, Cornell University, Ithaca, NY.

PANCHAPAKESAN, N. R. & LUMLEY, J. L. 1993 Turbulence measurements in axisymmetric jets of air and helium. Part 1. Air jet. *J. Fluid Mech.* **246**, 197–223.

PENG, D. 1985 Hot wire measurements in a momentum conserving axisymmetric jet. MS thesis, University at Buffalo, SUNY.

REICHARDT, H. 1941 Gesetzmassjkeiter der freien Turbulenz. *Z. angew. Math. Mech.* **36**, 526–529.

RICOU, F. P. & SPALDING, D. B. 1961 Measurements of entrainment by axisymmetric jets. *J. Fluid Mech.* **11**, 21–32.

RODI, W. 1975*a* A review of experimental data of uniform density free turbulent boundary layers. In *Studies in Convection* (ed. B. E. Launder), pp. 79–165. Academic.

RODI, W. 1975*b* New method of analyzing hot-wire signals in highly turbulent flow and its evaluation in round jets. *Disa Info.* **17**, 9–18.

SCHNEIDER, W. 1985 Decay of momentum flux in submerged jets. *J. Fluid Mech.* **154**, 91–110.

SEIF, A. A. 1981 Higher order closure model for turbulent jets. PhD dissertation, University at Buffalo, SUNY.

TAULBEE, D. B. 1989 Engineering turbulence models. A state-of-the-art review. *Advances in Turbulence* (ed. W. K. George & R. E. A. Arndt), pp. 10.5.1–10.5.6. Hemisphere.

TAULBEE, D. B., HUSSEIN, H. J. & CAPP, S. P. 1987 The round jet experiment and inferences on turbulence modelling. *Proc. of 6th Symp. on Turbulent Shear Flows*, Toulouse, France.

TENNEKES, H. & LUMLEY, J. L. 1972 *A First Course in Turbulence.* MIT Press, Cambridge, MA.

TOLLMIEN, W. 1926 Berechnung Turbulenter Ausbreitunsvorgange. *Z. angew. Math. Mech.* **6**, 468–478.

TOWNSEND, A. A. 1976 *The Structure of Turbulent Shear Flows*, 2nd edn. Cambridge University Press.

TUTU, N. & CHEVRAY, R. 1975 Cross-wire anemometry in high intensity turbulence. *J. Fluid Mech.* **71**, 785–800.

WYGNANSKI, I. & FIEDLER, H. E. 1969 Some measurements in the self-preserving jet. *J. Fluid Mech.* **38**, 577–612.